

The SOFIA Massive (SOMA) Radio Survey. II. Radio Emission from High-Luminosity Protostars

FRANCISCO SEQUEIRA-MURILLO,¹ VIVIANA ROSERO,^{2,3,4} JOSHUA MARVIL,³ JONATHAN C. TAN,^{5,6} RUBEN FEDRIANI,^{7,5}
YICHEN ZHANG,^{8,6} AZIA ROBINSON,⁹ PRASANTA GORAI,^{10,11} KEI E. I. TANAKA,¹² JAMES M. DE BUIZER,¹³
MARIA T. BELTRÁN,¹⁴ AND RYAN D. BOYDEN⁶

¹*Department of Astronomy, University of Wisconsin-Madison, 475 N. Charter St., Madison, WI 53703, USA*

²*Division of Physics, Mathematics, and Astronomy, California Institute of Technology, Pasadena, CA 91125, USA*

³*National Radio Astronomy Observatory, 1003 Lópezville Rd., Socorro, NM 87801, USA*

⁴*Space Science Institute, 4750 Walnut Street, Suite 205, Boulder, CO 80301, USA*

⁵*Department of Space, Earth & Environment, Chalmers University of Technology, 412 93 Gothenburg, Sweden*

⁶*Department of Astronomy, University of Virginia, Charlottesville, Virginia 22904, USA*

⁷*Instituto de Astrofísica de Andalucía, CSIC, Glorieta de la Astronomía s/n, 18008 Granada, Spain*

⁸*School of Physics and Astronomy, Shanghai Jiao Tong University, Shanghai, China*

⁹*Department of Physics and Astronomy, Agnes Scott College, 141 E. College Ave. Decatur, GA, 30030*

¹⁰*Roseland Centre for Solar Physics, University of Oslo, PO Box 1029 Blindern, 0315, Oslo, Norway*

¹¹*Institute of Theoretical Astrophysics, University of Oslo, PO Box 1029 Blindern, 0315, Oslo, Norway*

¹²*Department of Earth and Planetary Sciences, Institute of Science Tokyo, Meguro, Tokyo 152-8551, Japan*

¹³*Carl Sagan Center for Research, SETI Institute, Mountain View, CA, USA*

¹⁴*INAF-Osservatorio Astrofisico di Arcetri, Largo E. Fermi 5, I-50125 Firenze, Italy*

ABSTRACT

We present centimeter continuum observations of seven high luminosity massive protostars and their surroundings as part of the SOFIA Massive (SOMA) Star Formation Survey. With data from the Very Large Array and the Australia Telescope Compact Array, we analyze the spectral index, morphology and multiplicity of the detected radio sources. The high sensitivity and high resolution observations allow us to resolve many sources. We report thirteen new detections and two previously known detections that we observed for the first time in radio frequencies. We use the observations to build radio spectral energy distributions (SEDs) to calculate spectral indices. With radio morphologies and the spectral indices, we give assessments on the nature of the sources, highlighting five sources that display a radio jet-like morphology and a spectral index consistent with ionized jets. Combining with the SOMA Radio I sample, we present the radio - bolometric luminosity relation, especially probing the regime from $L_{\text{bol}} \sim 10^4$ to $10^6 L_{\odot}$. Here we find a steep rise in radio luminosity, which is expected by models that transition from shock ionization to photoionization.

Keywords: ISM: jets and outflows – stars: formation – techniques: interferometric

1. INTRODUCTION

Massive stars impact many processes in astrophysics, yet crucial aspects of their formation remain uncertain due to observational difficulties given by their relative rarity and large distances (typically > 1 kpc), crowded environments and high extinctions (Tan et al. 2014). Various theories have been proposed to explain the for-

mation of massive stars, but there is no general consensus on the basic nature of the formation mechanism. Theories range from the Turbulent Core Accretion (TCA) model (McKee & Tan 2003) to Competitive Accretion (e.g., Bonnell et al. 2001; Wang et al. 2010; Grudić et al. 2022) to Protostellar Collisions (Bonnell et al. 1998).

High-sensitivity centimeter continuum observations can provide valuable understanding of the earliest and most obscured phases of high-mass star formation. Tanaka et al. (2016) (hereafter TTZ16) developed models to predict the ionization structures and centimeter

continuum emission properties using initial parameters from a physical model based on TCA, including infall envelope, disk and outflow properties and their predicted thermal spectral energy distribution (SED) (Zhang & Tan 2011; Zhang et al. 2013, 2014b; Zhang & Tan 2018). Rosero et al. (2016, 2019b) demonstrated that many centimeter continuum sources have morphologies and parameters indicative of ionized jets, which is consistent with the results from the free-free emission models developed by TTZ16. This makes radio continuum emission highly relevant for constraining the ionizing luminosity of a protostar and helping to develop and test theoretical models for the evolutionary sequence of massive star formation.

In order to carry out such tests one needs a sample of massive protostars that ideally spans a range of core properties, evolutionary stages and environments. The SOFIA Massive (SOMA) Star Formation Survey (PI: J. Tan) was developed with such goals in mind. It aims to characterize a sample of ≥ 50 high and intermediate-mass protostars over a range of initial core masses, evolutionary stages and environments using SOFIA-FORCAST $\sim 10\text{--}40\ \mu\text{m}$ data. In Paper I of the survey (De Buizer et al. 2017) (hereafter SOMA I), the first eight sources were presented, which were mostly massive protostars. In Paper II (Liu et al. 2019) (hereafter SOMA II), seven high-luminosity sources were presented, representing some of the most massive protostars in the survey. In Paper III (Liu et al. 2020) (hereafter SOMA III), 14 intermediate-mass sources were presented. In Paper IV (Fedriani et al. 2023) (hereafter SOMA IV), 11 isolated sources, based on the $37\ \mu\text{m}$ imaging, were presented. In Paper V, Telkamp et al. (2025) (hereafter SOMA V) seven regions of relatively clustered massive star formation were studied.

The SOMA Radio Survey was developed with the goal of obtaining cm radio continuum observations of the SOMA sample, i.e., to have more comprehensive wavelength coverage of “extended spectral energy distributions” (E-SEDs) that constrains ionized gas properties and thus help break degeneracies that arise in infrared-only SED inferred properties from the standard SOMA analysis based on the Zhang & Tan (2018) (hereafter ZT18) TCA model grid. In SOMA Radio Paper I (Rosero et al. 2019a) (hereafter SOMA Radio I), the first eight sources of SOMA I were observed with the Karl G. Jansky Very Large Array (VLA) and the centimeter continuum data presented and analyzed, including comparison to the TTZ16 models for free-free emission.

In this paper, second in the radio series, we present ATCA and VLA data of the seven high-luminosity regions of SOMA II, containing a total of nine sources,

i.e., after adding IRAS 16562-3959 N and G305.20+0.21 A that were reported and analyzed in SOMA III.

Our approach follows the general methods developed in SOMA Radio I to analyze the data. In particular, we construct radio SEDs, by reducing the centimeter continuum observations, measuring the fluxes from the images, and analyzing the morphology and multiplicity of each source. We note that due to improvements in the infrared SED analysis, including a new algorithm to calculate the optimal aperture size in an unbiased and reproducible way for extended sources, updates in the SED fitting tool and revised methods assessing uncertainties in background subtracted fluxes, we use the infrared inferred results (e.g., bolometric luminosities) from SOMA V, rather than the results from SOMA II.

The paper is organized as follows: methodology and information regarding the observations are presented in §2. The observational results for each source are presented in §3, while the analysis and discussion of the sample are presented in §4. A summary and our conclusions are presented in §5.

2. METHODS

The SOMA Star Formation Survey sample is defined by SOFIA-FORCAST observations (i.e., from ~ 7 to $40\ \mu\text{m}$). The sample we analyze in this paper are part of the protostars presented by SOMA II, as well as sources IRAS 16562-3959 N and G305.20+0.21A that were reported in SOMA III, as an addendum to the sources in the SOMA II regions. Thus a total of nine protostars in seven target regions will be analyzed: G45.12+0.13, G309.92+0.48, G35.58-0.03, IRAS 16562-3959, IRAS 16562-3959 N, G305.20+0.21, G305.20+0.21 A, G49.27-0.34 and G339.88-1.26. The radio observations presented here are our own VLA observations for regions G45.12+0.13, G35.58-0.03 and G49.27-0.34. For G305.20+0.21 and G309.92+0.48 we present our own ATCA observations, and for regions IRAS 16562-3959 and G339.88-1.26, we used ATCA observations reported by Guzmán et al. (2016) and Purser et al. (2016), respectively.

The data analyzed in this work are summarized in Table 1. Column 1 gives region name; columns 2, 3, and 4 provide band frequency, R.A., and Decl., respectively; columns 5 and 6 give synthesized beam size and position angle (PA), and the rms of the resulting images. The distance, as adopted by SOMA II, as well as the bolometric luminosities and the isotropic bolometric luminosity evaluated by SOMA V, are shown in columns 7, 8 and 9, respectively. A list of phase calibrators used in the VLA observations at 1.3 and 6 cm is given in Table 2.

Table 1. SOMA Sources: Radio Continuum Data.

Region	Frequency Band	R.A.	Decl.	Beam Size	rms	d^c	$L_{\text{bol,iso}}^d$	L_{bol}^d
	(GHz)	(J2000)	(J2000)	("×", degree)	($\mu\text{Jy beam}^{-1}$)	(kpc)	(L_{\odot})	(L_{\odot})
G45.12+0.13 ^a	4.0 – 8.0	19 13 27.86	+10 53 36.6	0.26 × 0.25, −45.5	35	7.40	$4.4_{-2.2}^{+4.4} \times 10^5$	$8.0_{-3.6}^{+6.5} \times 10^5$
	18.0 – 26.0	0.33 × 0.25, −53.2	120
G309.92+0.48 ^b	5.5 – 9.0	13 50 41.85	−61 35 10.4	1.09 × 0.89, +12.3	560	5.50	$3.1_{-0.6}^{+0.8} \times 10^5$	$6.6_{-2.8}^{+4.8} \times 10^5$
	17.0 – 22.8	0.83 × 0.52, −11.1	820
G35.58-0.03 ^a	4.0 – 8.0	18 56 22.56	+02 20 27.7	0.32 × 0.27, +64.7	8	10.2	$2.4_{-0.3}^{+0.3} \times 10^5$	$4.3_{-1.7}^{+2.9} \times 10^5$
	18.0 – 26.0	0.30 × 0.29, +73.5	90
IRAS 16562-3959 ^{b†}	5.0 – 9.0	16 59 41 63	−40 03 43.6	2.49 × 1.36, −4.13	21	1.70	$4.9.0_{-1.3}^{+1.9} \times 10^4$	$2.2_{-1.2}^{+2.5} \times 10^5$
	17.0 – 19.0	0.78 × 0.39, +2.87	28
G305.20+0.21 ^b	5.5 – 9.0	13 11 10.49	−62 34 38.8	0.97 × 0.82, +86.5	70	4.10	$6.2_{-1.4}^{+1.7} \times 10^4$	$2.1_{-1.0}^{+2.0} \times 10^5$
	17.0 – 22.8	0.61 × 0.40, −6.59	70
G49.27-0.34 ^a	4.0 – 8.0	19 23 06.61	+14 20 12.0	0.29 × 0.26, +64.3	6	5.55	$1.4_{-0.9}^{+2.8} \times 10^5$	$1.0_{-0.3}^{+0.5} \times 10^5$
	18.0 – 26.0	0.33 × 0.26, −62.2	9
G339.88-1.26 ^{b‡}	5.5 – 9.0	16 52 04.67	−46 08 34.2	2.38 × 1.44, −16.3	25	2.10	$3.8_{-1.1}^{+1.6} \times 10^4$	$9.1_{-5.8}^{+16.0} \times 10^4$
	17.0 – 22.8	0.90 × 0.34, −1.09	75

NOTE— Units of R.A. are hours, minutes, and seconds. Units of Decl. are degrees, arcminutes, and arcseconds.

^a Images from the VLA.

^b Images from ATCA.

^c References cited in SOMA II.

^d Average and dispersion of the bolometric luminosities of the good models from SOMA V, these values and other intrinsic properties are reported in Table C1.

[†] Images obtained from Andrés Guzmán (via public personal archive).

[‡] Images obtained from Simon Purser (via private communication).

Table 2. VLA Calibrators.

Calibrator	Astrometry Precision ^a	Source Calibrated	Band
J1922+1530	A	G45.12+0.13	C
J1924+1540	A	G45.12+0.13	K
J1824+1044	A	G35.58-0.03	C
J1851+0035	C	G35.58-0.03	K
J1922+1530	A	G49.27-0.34	C
J1925+2100	A	G49.27-0.34	K

NOTE—

^a Astrometric precisions of A, B and C correspond to positional accuracies of <0.002 arcsec, 0.002–0.01 arcsec and 0.01–0.15 arcsec, respectively.

2.1. VLA data

2.1.1. The 6 cm data

The 6 cm (C-Band) observations were carried out in the A configuration providing angular resolutions $\sim 0''.3$. The project code for the observations of regions G35.58-0.03 and G49.27-0.34 is 18A-294 (PI: V. Rosero) and for region G45.12+0.13 is 19A-216 (PI: V. Rosero). The

data consists of two ~ 2 GHz wide basebands (3 bit samplers) centered at 5.03 and 6.98 GHz. The data were recorded in 30 unique spectral windows (SPWs), each comprised of 64 channels and each channel being 2 MHz wide, resulting in a total bandwidth of 3842 MHz (before “flagging”). Source 3C48 was used as flux density and bandpass calibrator for regions G35.58-0.03 and G49.27-0.34, and 3C286 for region G45.12+0.13.

The data were processed using NRAO’s Common Astronomy Software Applications (CASA) package and we use calibrated data from the VLA Calibration Pipeline version 41154 (Pipeline-CASA51-P2-B) for regions G35.58-0.03 and G49.27-0.34, and the VLA Calibration Pipeline version 42270 (Pipeline-CASA54-P2-B) for region G45.12+0.13. The images were made using the *tclean* task and Briggs *Robust* = 0.5 weighting (Briggs 1995). Imaging of regions G35.58-0.03 and G45.12+0.13 also included one round of phase-only self calibration using solution intervals ranging from 30s to 60s depending on frequency.

For all the regions we made two images, each of a ~ 2 GHz baseband composed of 15 SPWs, and also a combined image using data from both basebands with a total of 30 SPWs. All maps were primary beam-corrected. Columns 5 and 6 of Table 1 list the synthesized beam

Table 3. Observation times for sources observed using the VLA.

Source	Band	Phase		Total
		Source ^a	Calibrator ^a	Integration
		(min)	(min)	(min)
G45.12+0.13	C	8.4	0.45	42
	K	1.2	0.54	23
G35.58-0.03	C	8.2	0.52	41
	K	2.5	0.62	23
G49.27-0.34	C	8.6	0.65	43
	K	2.3	0.51	20

NOTE—

^a Alternating time from source to calibrator.

(size and position angle) and the rms of the combined images.

Table 3 shows approximations of the observation times for each region at both 6 and 1.3 cm bands. All the observations were made alternating between the target source and the phase calibrator. Columns 3 and 4 show these alternating times, and column 5 shows the total on source integration time for each observation.

2.1.2. The 1.3 cm data

The 1.3 cm (K-Band) observations were made in the B configuration providing angular resolutions $\sim 0''.4$. The project code for all observations in this band is 19A-216 (PI: V. Rosero). The data consists of two ~ 4 GHz wide basebands (3 bit samplers) centered at 20.4 and 24.4 GHz. The data was recorded in 60 unique SPWs, comprised of 64 channels and each channel being 2 MHz wide, resulting in a total bandwidth of 7680 MHz, before “flagging”. Source 3C286 was used as flux density and bandpass calibrator. The data reduction was done in the same manner as that for the C-Band observations, using the VLA Calibration Pipeline version 42270 (Pipeline-CASA54-P2-B) for all the regions.

The images were made using the *tclean* task and Briggs *Robust* = 0.5 weighting. We made two images, each of a ~ 4 GHz baseband composed of 30 SPWs, and also a combined image using data from both basebands with a total of 60 SPWs. All maps were primary beam-corrected. Columns 5 and 6 of Table 1 show the synthesized beam (size and position angle) and the rms of the combined images.

2.2. ATCA data

For regions G309.92+0.48, IRAS 16562-3959, G305.20+0.21 and G339.88-1.26 we used ATCA data. The project code of the observations for the regions G309.92+0.48 and G305.20+0.21 is C3396 (PI: V. Rosero). For regions IRAS 16562-3959 and G339.88-1.26, we used ATCA observations reported by Guzmán et al. (2016) and Purser et al. (2016).

The observations from project code C3396 were made using ATCA in the 6A and 6B configurations on October 2020. Observations were made at four frequencies: 5.5, 9.0, 17.0 and 22.8 GHz, each with a bandwidth of 2048 MHz (XX, YY, XY, and YX polarizations) that was split into channels of width 1 MHz.

Individual scan times on flux and phase calibrators were 5 minutes and 90 seconds respectively and on target sources were between 3 and 45 minutes dependent on atmospheric conditions and observing frequencies. The average total integration time on each science target was 75 minutes. The bandpass and flux density was calibrated with source B1934-638 using the Stevens-Reynolds 2016 model (Partridge et al. 2016). The ATCA data were calibrated in CASA following standard interferometric procedures for flagging, flux-density transfer and phase referencing. Imaging of region G305.20+0.21 also included one round of phase-only self calibration using solution intervals ranging from 30s to 60s depending on frequency.

For the two regions observed with project code C3396 we made four images centered around the four frequencies previously described. However, similarly to the VLA observations, we also made two additional images with the combined data at the lowest frequency observations (5.5 and 9.0 GHz) and at the highest frequency observations (17 and 22.8 GHz). This resulted in two frequency-combined radio maps centered around 7.2 and 19.9 GHz respectively.

For region IRAS 16562-3959 we used the data from Guzmán et al. (2016) at 5, 9, 17 and 19 GHz: more information about the observations can be found in section 2 of their paper. Meanwhile, for region G339.88-1.26 we used data from Purser et al. (2016) at 5.5, 9.0, 17.0 and 22.8 GHz: more information about the observations can be found in section 3.1 of their paper. In order to have frequencies comparable to the combined images made for the other sources, we select the lowest and highest frequency maps of both regions for use in the direct comparison with the combined maps.

3. RESULTS

Following the methods of SOMA Radio I, we consider a radio source being detected when the peak intensity I_ν is at least 5 times the rms (σ) in either of the baseband-

combined images (see Section 2.1 and 2.2) at the different frequencies. For non-detections in the combined images, we report a 3σ limiting value for the flux density at a given frequency.

Figure 1 shows the radio contour plots of the lower frequency in red (C-band (6 cm) for the VLA observations and 5, 5.5 or 7.2 GHz for ATCA observations) and the higher frequency in cyan (K-band (1.3 cm) for the VLA observations and 17, 19 or 19.9 GHz for ATCA observations) for all the radio sources detected in our sample and overlaid to SOFIA-FORCAST 37 μm images.

The blue circles represent the SOMA aperture set by SOMA IV using the automated algorithm to choose the optimal aperture size (see Table C1 of SOMA V), except for IRAS 16562-3959 N, where the aperture radius is set from the 37.1 μm image reported by SOMA III (see Table 2 of SOMA III), this aperture size was used to build the IR SEDs. The infrared images presented in SOMA II (including SOFIA, Herschel, and Spitzer data) and the VLA data presented here have astrometric accuracies better than $1.5''$ and $0''.1$ (see Table 2), respectively. Meanwhile, the ATCA data presented here have astrometric accuracies better than $0''.4$, including both the phase calibrator’s positional uncertainty and errors in transferring phases to the target.

Tables 4-12 report the radio parameters for each of the nine protostars studied in this paper. These parameters were measured based on different size scales, as follows. The SOMA scale refers to the size of the aperture radius used in SOMA II and SOMA V to measure IR fluxes. The *Intermediate* scale is based on the morphology of the radio source, specifically whether the detections appear to be of jet-like nature. The *Inner* scale is given by the size of the central radio detection that is likely most closely associated with the driving protostar (i.e., association with compact millimeter dust continuum emission). For the VLA data presented, we determined the flux density S_ν in each wideband image in the

SOMA and *Intermediate* scales by using the task *imstat* of CASA, either enclosing the SOMA aperture in a circular region or enclosing the elongated jet-like structure in a box, respectively (see Table 13). The uncertainties of the flux densities for these two scales are estimated as $\sigma_{\text{image}}(\text{npts}/\text{beam area})^{0.5}$ added in quadrature with an assumed 10% error in calibration, where σ_{image} is the rms of the image, npts is the number of pixels enclosed in the box or the circular region, and the beam area is the number of pixels within a synthesized beam of the image. For the *Inner* scale, we determined the flux density using the task *imfit* of CASA, and the uncertainty was estimated using the statistical error from the Gaussian fit added in quadrature with an assumed 10% error in calibration.

Column 1 of Tables 4-12 shows the given scale; for each, columns 2 and 3 report the R.A. and Decl. For the SOMA scale, these refer to the pointing center observations of SOFIA-FORCAST (see SOMA II Table 1); for the *Intermediate* scale, they refer to a middle point in the jet-like detection; and for the *Inner* scale, they refer to the R.A. and Decl. of the peak intensity of the central detected object. The following columns are the flux densities (S_ν) at different frequencies, with the uncertainties given in parentheses (for non-detections, the upper limits denotes the minimum detectable flux of a point source). The last column in Tables 4-12 report the spectral indices and their uncertainties at each scale (see Section 3.2). Since the radio data are not sensitive to extended emission over scales as large as the SOMA and possibly the *Intermediate* scales, the flux measurements represent the sum over all compact sources within the scale, and the spectral indices contain some corresponding uncertainty (more details in Section 3.2). The error bars for these measurements are large, due to having many independent beams within the scale.

Table 4. G45.12+0.13: Parameters from Radio Continuum.

Scale	R.A.	Decl.	$S_{5.0 \text{ GHz}}$	$S_{7.0 \text{ GHz}}$	$S_{20.4 \text{ GHz}}$	$S_{24.4 \text{ GHz}}$	Spectral
	(J2000)	(J2000)	(mJy)	(mJy)	(mJy)	(mJy)	Index
SOMA	19:13:27.86	+10:53:36.60	1797.44(180.6)	1855.93(186.5)	3673.00(367.5)	3593.19(360.71)	0.5(0.1)
<i>Intermediate</i>
<i>Inner</i>	19:13:27.87	+10:53:36.17	1702.69(51.11)	1928.91(57.89)	3668.96(110.0)	3722.08(111.7)	0.5(0.1)

NOTE—Units of R.A. are hours, minutes, and seconds. Units of Decl. are degrees, arcminutes, and arcseconds.

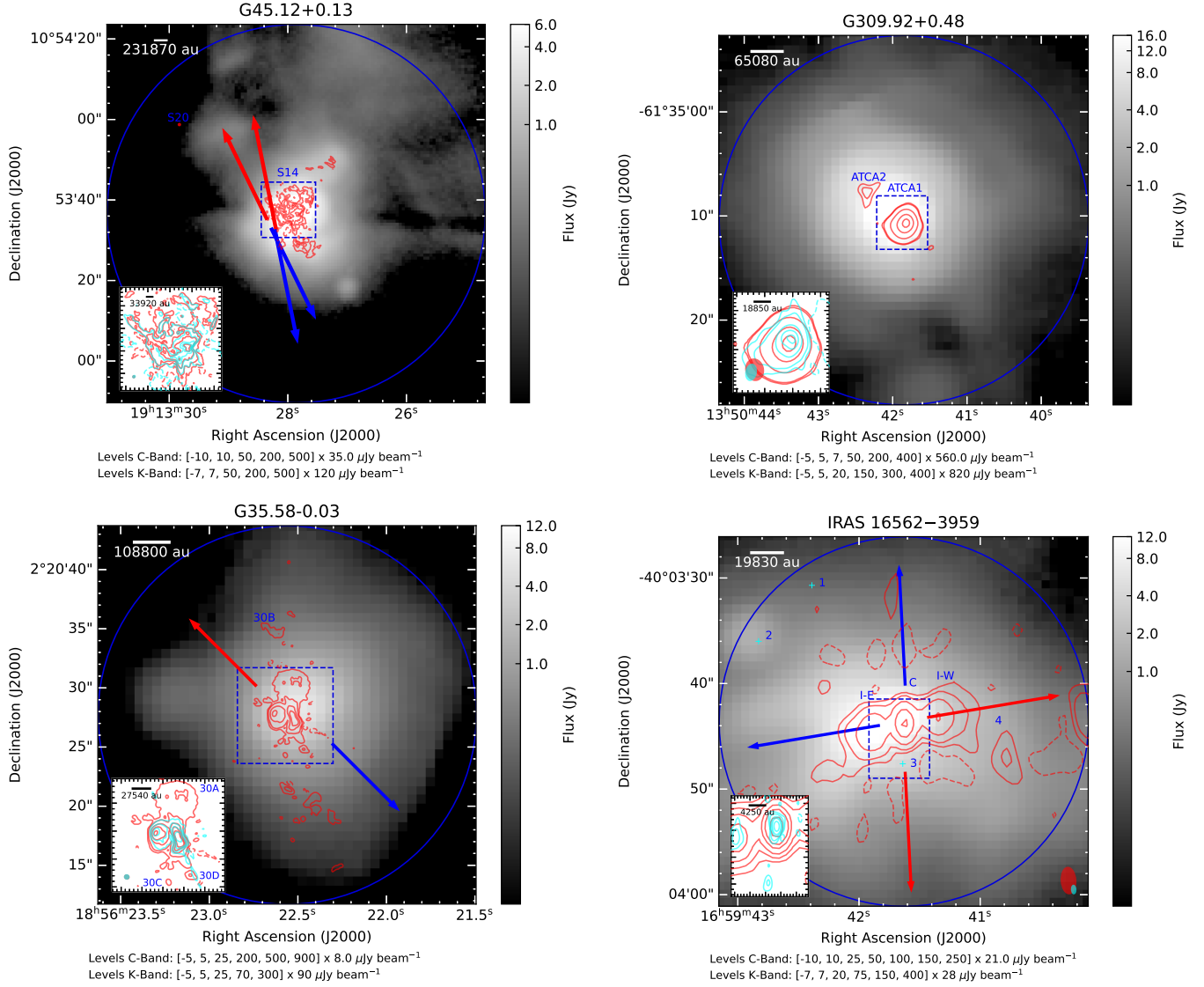


Figure 1. Images are SOFIA-FORCAST $37\ \mu\text{m}$ with VLA contours – red: lower frequency (C-band (6 cm) for the VLA observations and 5, 5.5 or 7.2 GHz for ATCA observations); cyan: (K-band (1.3 cm) for the VLA observations and 17, 19 or 19.9 GHz for ATCA observations) – of the combined radio maps overlaid. The cyan crosses in IRAS 16562–3959 denotes the position of detections only at the high frequency bands (cyan contours). The blue dashed squares correspond to the area of the inset image showing a zoom-in of the central region, and the synthesized beams are shown in the lower corners of these insets. The blue circles are the SOMA apertures used by **SOMA V** and reported in Table C1, except for IRAS 16562-3959 N where we use the SOMA aperture from **SOMA II** reported in their Table 2. The aperture radius is defined using the optimal aperture size algorithm developed by **SOMA IV**, except for IRAS 16562-3959 N, which is defined from the $37.1\ \mu\text{m}$ emission. The blue and red arrows represent the direction of a molecular outflow detected toward the region, only in regions with known molecular outflows (more details in Section 3.1). A scale bar in units of au is shown in the upper left of the figures.

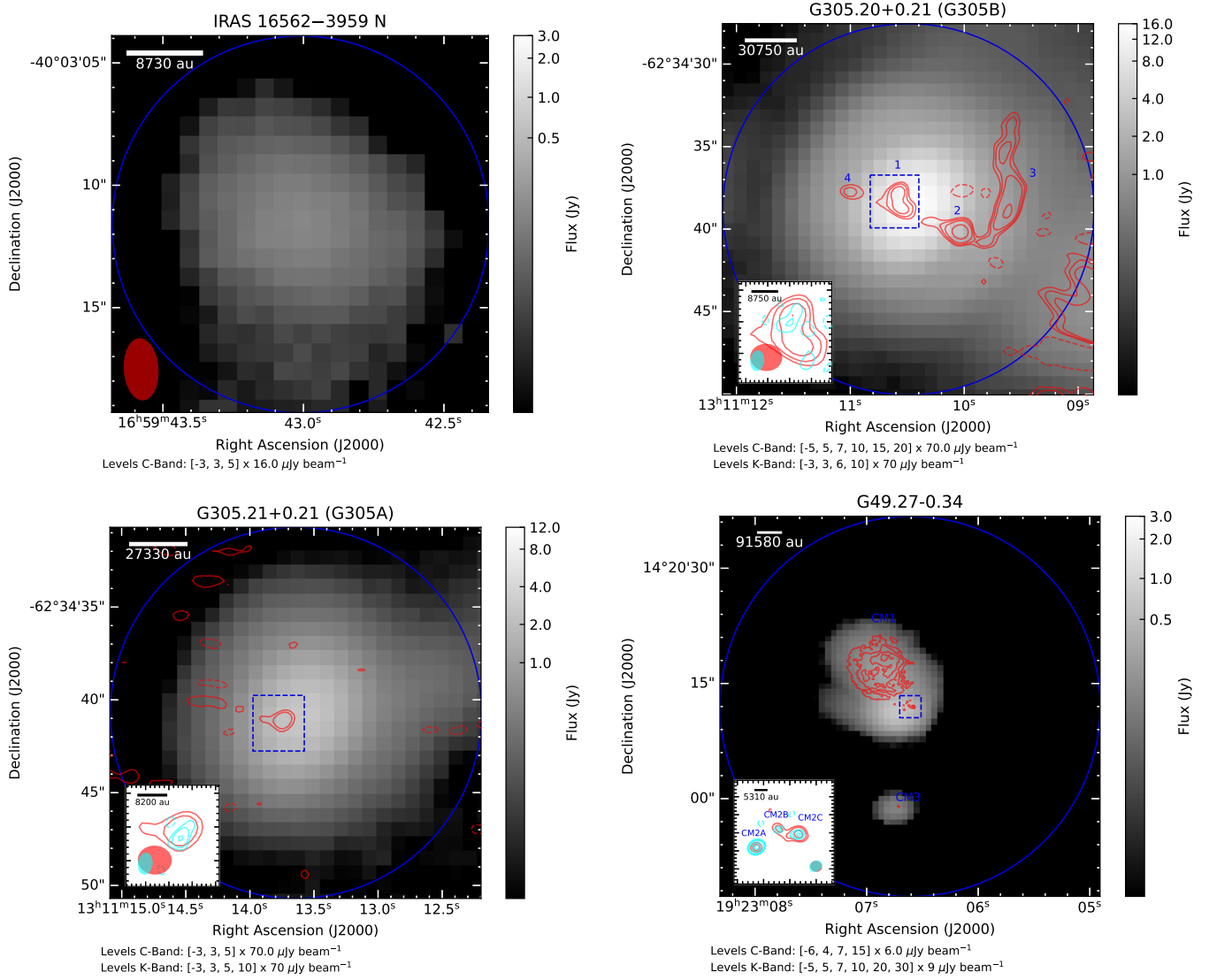


Figure 1. (Continued)

Table 5. G309.92+0.48: Parameters from Radio Continuum.

Scale	R.A.	Decl.	$S_{5.5 \text{ GHz}}$	$S_{9.0 \text{ GHz}}$	$S_{17.0 \text{ GHz}}$	$S_{22.8 \text{ GHz}}$	Spectral
	(J2000)	(J2000)	(mJy)	(mJy)	(mJy)	(mJy)	Index
SOMA	13:50:41.85	-61.35:10.40	454.76(47.4)	753.47(79.0)	1017.68(108.6)	955.54(115.6)	0.5(0.1)
<i>Intermediate</i>
<i>Inner</i>	13:50:41.84	-61.35:10.85	428.18(14.6)	713.91(29.3)	1085.90(57.86)	1191.15(76.69)	0.7(0.1)

NOTE—Units of R.A. are hours, minutes, and seconds. Units of Decl. are degrees, arcminutes, and arcseconds.

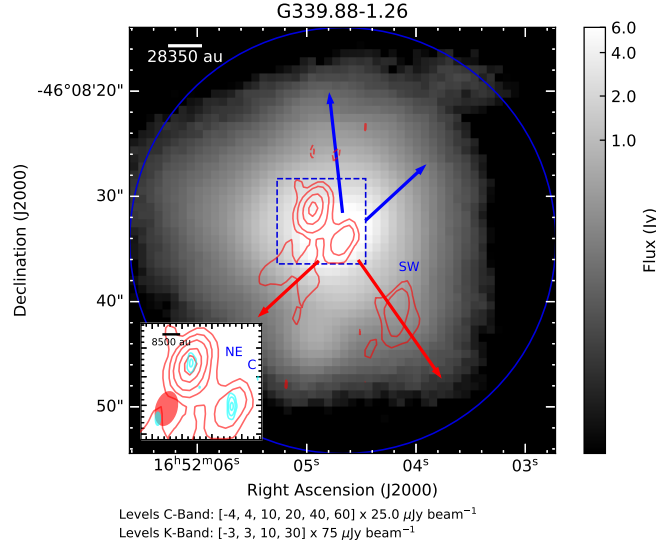


Figure 1. (Continued)

Table 6. G35.58-0.03: Parameters from Radio Continuum.

Scale	R.A. (J2000)	Decl. (J2000)	$S_{5.0}$ GHz (mJy)	$S_{7.0}$ GHz (mJy)	$S_{20.4}$ GHz (mJy)	$S_{24.4}$ GHz (mJy)	Spectral Index
SOMA	18:56:22.52	+02.20.27.20	172.38(17.3)	199.20(20.0)	302.12(30.6)	321.61(33.5)	0.4(0.1)
<i>Intermediate</i>
<i>Inner</i> ^a	18:56:22.52	+02.20.30.53	84.00(27.32)	118.00(35.05)	237.00(91.14)	263.00(101.47)	0.7(0.2)

NOTE—The Intermediate scale corresponds to the extent of the radio jet. Units of R.A. are hours, minutes, and seconds. Units of Decl. are degrees, arcminutes, and arcseconds.

^a Inner scale corresponds to source 30 that we are resolving into sources 30N and 30S (see section 3.1.3 and Table 14 for more details).

Table 7. IRAS 16562-3959: Parameters from Radio Continuum.

Scale	R.A. (J2000)	Decl. (J2000)	$S_{5.0}$ GHz (mJy)	$S_{9.0}$ GHz (mJy)	$S_{17.0}$ GHz (mJy)	$S_{19.0}$ GHz (mJy)	Spectral Index
SOMA	16:59:41.63	-40.03.43.60	18.92(1.9)	23.50(2.4)	34.27(3.7)	31.56(3.5)	0.4(0.1)
<i>Intermediate</i>	16:59:42.17	-40.03.46.85	19.66(2.0)	27.63(2.8)	31.84(3.2)	33.34(3.4)	0.4(0.1)
<i>Inner</i>	16:59:41.63	-40.03.43.73	8.18(0.87)	13.40(1.43)	20.80(2.19)	22.90(2.43)	0.8(0.1)

NOTE—Units of R.A. are hours, minutes, and seconds. Units of Decl. are degrees, arcminutes, and arcseconds.

Table 8. IRAS 16562-3959 N: Parameters from Radio Continuum.

Scale	R.A.	Decl.	$S_{5.0 \text{ GHz}}$	$S_{9.0 \text{ GHz}}$	$S_{17.0 \text{ GHz}}$	$S_{19.0 \text{ GHz}}$	Spectral
	(J2000)	(J2000)	(mJy)	(mJy)	(mJy)	(mJy)	Index
SOMA	16:59:43.01	-40.03.11.56	<0.39	0.47(0.22)	0.59(0.64)	0.87(0.66)	<0.7
<i>Intermediate</i>
<i>Inner</i>	<0.06	<0.06	<0.09	<0.08	<0.4

NOTE—Units of R.A. are hours, minutes, and seconds. Units of Decl. are degrees, arcminutes, and arcseconds.

Table 9. G305.20+0.21 (G305B): Parameters from Radio Continuum.

Scale	R.A.	Decl.	$S_{5.5 \text{ GHz}}$	$S_{9.0 \text{ GHz}}$	$S_{17.0 \text{ GHz}}$	$S_{22.8 \text{ GHz}}$	Spectral
	(J2000)	(J2000)	(mJy)	(mJy)	(mJy)	(mJy)	Index
SOMA	13:11:10.49	-62.34.38.80	16.57(2.11)	12.98(2.36)	3.42(2.63)	<29.72	<-1.0
<i>Intermediate</i>	13:11:10.52	-62.34.39.08	7.23(0.83)	4.55(0.77)	1.59(0.83)	<9.33	<-1.2
<i>Inner</i>	13:11:10.56	-62.34.38.31	3.39(0.13)	1.61(0.89)	1.37(0.19)	1.92(0.38)	-0.7(0.2)

NOTE—Units of R.A. are hours, minutes, and seconds. Units of Decl. are degrees, arcminutes, and arcseconds.

Table 10. G305.21+0.21 (G305A): Parameters from Radio Continuum.

Scale	R.A.	Decl.	$S_{5.5 \text{ GHz}}$	$S_{9.0 \text{ GHz}}$	$S_{17.0 \text{ GHz}}$	$S_{22.8 \text{ GHz}}$	Spectral
	(J2000)	(J2000)	(mJy)	(mJy)	(mJy)	(mJy)	Index
SOMA	13:11:13.64	-62.34.40.70	1.25(2.37)	1.05(2.14)	0.71(2.18)	3.22(8.43)	-0.3(3.1)
<i>Intermediate</i>
<i>Inner</i>	13:11:13.75	-62.34.41.31	0.96(0.01)	0.74(0.04)	0.91(0.09)	2.70(0.27)	0.2(0.2)

NOTE—Units of R.A. are hours, minutes, and seconds. Units of Decl. are degrees, arcminutes, and arcseconds.

Table 11. G49.27-0.34: Parameters from Radio Continuum.

Scale	R.A.	Decl.	$S_{5.0 \text{ GHz}}$	$S_{7.0 \text{ GHz}}$	$S_{20.4 \text{ GHz}}$	$S_{24.4 \text{ GHz}}$	Spectral
	(J2000)	(J2000)	(mJy)	(mJy)	(mJy)	(mJy)	Index
SOMA	19:23:06.61	+14.20.12.00	44.30(4.54)	52.93(5.44)	26.11(3.34)	40.86(4.50)	-0.3(0.1)
<i>Intermediate</i>	19:23:06.69	+14.20.11.22	0.21(0.04)	0.01(0.04)	0.33(0.08)	0.34(0.07)	0.7(0.5)
<i>Inner</i>	19:23:06.66	+14.20.11.66	0.04(0.01)	0.03(0.01)	0.27(0.02)	0.35(0.02)	1.6(0.2)

NOTE—Units of R.A. are hours, minutes, and seconds. Units of Decl. are degrees, arcminutes, and arcseconds.

Table 12. G339.88-1.26: Parameters from Radio Continuum.

Scale	R.A.	Decl.	$S_{5.5 \text{ GHz}}$	$S_{9.0 \text{ GHz}}$	$S_{17.0 \text{ GHz}}$	$S_{22.8 \text{ GHz}}$	Spectral
	(J2000)	(J2000)	(mJy)	(mJy)	(mJy)	(mJy)	Index
SOMA	16:52:04.67	-46.08.34.20	5.50(0.71)	3.64(0.68)	4.11(2.16)	4.27(4.61)	-0.6(0.5)
<i>Intermediate</i>	16:52:04.62	-46.08.36.04	5.31(0.57)	6.86(0.73)	4.58(1.04)	4.03(2.05)	-0.1(0.2)
<i>Inner</i>	16:52:04.94	-46.08.31.32	0.86(0.09)	1.51(0.16)	2.44(0.26)	3.00(0.33)	0.9(0.1)

NOTE—Units of R.A. are hours, minutes, and seconds. Units of Decl. are degrees, arcminutes, and arcseconds.

Table 13. Size scales of flux measurements.

Region	SOMA	Intermediate	Inner
	R (")	w (") \times h (")	a (") \times b (")
G45.12+0.13	47.0	...	3.67×2.33^a
G309.92+0.48	17.75	...	1.96×1.75^a
G35.58-0.03	16.0	...	2.88×0.50^a
IRAS 16562-3959	17.5	13.2×6.82	2.46×1.61^a
IRAS 16562-3959 N	7.7
G305.20+0.21	11.25	8.68×4.45	1.12×0.77^a
G305.20+0.21 A	10.0	...	1.16×1.11^a
G49.27-0.34	24.75	2.01×1.14	0.44×0.37^b
G339.88-1.26	20.25	13.8×17.9	2.38×0.91^a

NOTE—The reported values correspond to a circle of radius R for the SOMA scale and a box of height h and width w for the *Intermediate* scale. In some cases the inner scale between the C and K images are different so we report the larger area that we consider any source of emission within the inner region, we also have two different types of regions:

^a Scale corresponds to image component (convolved with beam) size from the task imfit, of major axis a and minor axis b .

^b Scale corresponds to an ellipse of major axis a and minor axis.

3.1. Morphology and Multiplicity

All the target regions presented in this paper have been observed in the centimeter continuum. We describe source morphology as “compact” if the detection shows no structure on the scale of a few synthesized beams or greater. Otherwise we describe it as “extended”. Below, we describe the centimeter wavelength detections toward each target; for a detailed literature review on each of these regions, see [SOMA II](#).

3.1.1. G45.12+0.13

G45.12+0.13 is a massive star-forming region, also known as IRAS 19111+1048, that is associated with an UC HII region. It is located at 7.4 kpc ([Ginsburg et al. 2011](#)) and is part of the Galactic Ring Survey Molecular Cloud (GRSMC) G45.46+0.05, a large star formation complex ([Wood & Churchwell 1989](#); [Simon et al. 2001](#)).

G45.12+0.13 has been analyzed at multiple wavelengths ranging from IR, sub-mm and radio ([Hunter et al. 1997](#); [Vig et al. 2006](#); [Azatyan et al. 2022](#)). [Hunter et al. \(1997\)](#) reported bipolar outflows towards this region using CO ($J = 6-5$) maps. From this study, the highest velocity outflow is centered around a source termed S14, while an additional outflow is centered around another UC HII region source G45.12+0.13 West. Both of these UC HII regions contain type-I OH masers ([Argon et al. 2000](#)). Additionally, with radio observations from the Giant Metrewave Radio Telescope (GMRT) at 1280, 610 and 325 MHz, [Vig et al. \(2006\)](#) suggested that this region shows a highly homogeneous ionized medium morphology and [SOMA II](#) confirm this morphology with their MIR images. Furthermore, [Vig et al. \(2006\)](#) concluded that G45.12+0.13 contains a cluster of ZAMS stars energizing a compact and evolved HII region. In total they reported 20 sources, with S14 being the central UC HII source and S20 a non-thermal source according to its radio emission.

From our VLA observations at 1.3 and 6 cm we report two detections corresponding to sources S14 and S20 from [Vig et al. \(2006\)](#). Both detections have an offset in the peak intensity position from the results of [Vig et al. \(2006\)](#) using GMRT observations, by a difference of around $2.1''$ to the SE (see [Figure 2](#)). This systematic offset may be due to astrometric uncertainties in the GMRT data.

It is important to highlight that despite our data being of higher resolution, we only detect two of the twenty compact sources from the cluster reported by [Vig et al. \(2006\)](#). From our data we infer that most of the emission to the northern side of the central UC HII region arises

from an extended and diffuse irregular cloud of ionized material instead of a cluster of compact sources.

In order to confirm our results, we produce an image using shorter baseline observations from the VLA archive (project code 20A-519; PI: David Neufeld) at L-band (1.5 GHz) in order to compare the results with the 1.28 GHz image from [Vig et al. \(2006\)](#). Figure 2 shows this L-band continuum image with overlaid C, K and L-band VLA contours. The positions of the cluster of point sources reported by [Vig et al. \(2006\)](#) at 1280 MHz are marked with a white \times symbols.

Based on these results, we clearly see that from our images at 1.3 and 6 cm (see Figure 1), the diffuse ionized material has been filtered out by the long baselines, hence we only detect the very compact point source S20 and the most inner part of the UC HII region source S14. Furthermore, from the shorter baseline image we infer that most of the emission to the north west of the central UC HII region arises from an extended and diffuse irregular cloud of ionized material instead of a cluster of compact sources.

From our VLA observations, source S14 is located at R.A.(J2000) = $19^h 13^m 27^s.87$, Decl.(J2000) = $+10^\circ 53' 36.''2$ with a spectral index of 0.5. S14 presents a very complex morphology, and in fact at the shorter frequency (L-band) it appears to have an hour-glass morphology, as seen in the right plot of Figure 2. This observed morphology is similar to the one detected towards source G45.47+0.05 by [Zhang et al. \(2019a\)](#), who interpreted this as arising from a photoionized outflow. Furthermore, the molecular outflows observed towards G45.12+0.13 (see Figure 1) are consistent with the direction of the axis of the hour-glass of source S14. Meanwhile S20 is located at R.A.(J2000) = $19^h 13^m 29^s.83$, Decl.(J2000) = $+10^\circ 53' 58.''7$ with a spectral index of -0.9 , a value that is consistent with the non-thermal detection made by [Vig et al. \(2006\)](#). S20 presents a very compact morphology at both frequency bands.

3.1.2. *G309.92+0.48*

G309.92+0.48 or IRAS 13471-6120 is a region located at 5.5 kpc ([Murphy et al. 2010](#)). It is associated with OH and methanol masers, as well as radio continuum emission from an UC HII region at 8.6 and 19 GHz ([Caswell 1997](#); [Phillips et al. 1998](#); [Walsh et al. 1998](#)). In the MIR, G309.92+0.48 is resolved into several sources: [De Buizer et al. \(2000\)](#) reported it to be composed of a total of 6 point sources (labeled 1 to 6) using high resolution ($\sim 0.3''$) 11.7 μm data from *Gemini* (see also [SOMA II](#)).

From our ATCA observations, we have detected two sources that we name ATCA1 and ATCA2 (see Figure 1). Source ATCA1 is detected at all frequencies (5.5, 9, 17, and 22.8 GHz) and source ATCA2 is only detected at the lower frequencies (5.5 and 9 GHz). Both sources are consistent with the previously reported sources by [Phillips et al. \(1998\)](#) at 8.6 GHz, sources that are associated with the MIR sources 1 and 2. [Murphy et al. \(2010\)](#) presented radio continuum observations at 20 GHz towards this region, detecting only source ATCA1, which is consistent with our results of non-detection for source ATCA2 at higher frequencies.

ATCA1 is a slightly elongated source located at R.A.(J2000) = $13^h 50^m 41^s.84$, Decl.(J2000) = $-61^\circ 35' 10.''8$ and we report a spectral index of 0.7. ATCA2 is located at R.A.(J2000) = $13^h 50^m 42^s.29$, Decl.(J2000) = $-61^\circ 35' 07.''7$ with a spectral index of -0.7 . Both of these sources show a similar morphology to the previous radio observations mentioned above.

For ATCA1, [Murphy et al. \(2010\)](#) presented a spectral index of 1.2 between 20 GHz and 0.843 GHz. Our estimated spectral index value is different (~ 0.7), but still both results fall into the range of a typical UC HII region. ATCA2 shows non-thermal emission given the negative value in the spectral index. No molecular outflows have been detected towards this region.

3.1.3. *G35.58-0.03*

G35.58-0.03 (hereafter G35.58) is a star-forming region located at a kinematic distance of 10.2 kpc ([Watson et al. 2003](#)). G35.58 has been resolved into two UC HII regions (from now on called sources 30 and 31) using 2 and 3.6 cm observations, where water and OH masers have been detected towards source 30 ([Kurtz et al. 1994](#); [Caswell et al. 1995](#)). Additionally, [Zhang et al. \(2014a\)](#) shows evidence of an ionized outflow driving a NE-SW molecular outflow centered in source 30.

With high-resolution 11.7 μm *Gemini* observations, [SOMA II](#) resolved the MIR emission into a main bright peak with two extended diffuse emissions to the north and the northwest. The main bright peak is associated with the eastern UC HII region (source 31).

We present 6 and 1.3 cm observations of this region, where we detect twelve sources at different evolutionary stages. Most of these sources are only detected at C band with a few sources being detected at both frequency bands (30A, 30E, 30N, 30S and 31). Table 14 shows the information about the multiplicity in G35.58, such as the R.A. and Decl. positions, the estimated spectral indices, association with other wavelengths and whether the source is a new radio detection or not.

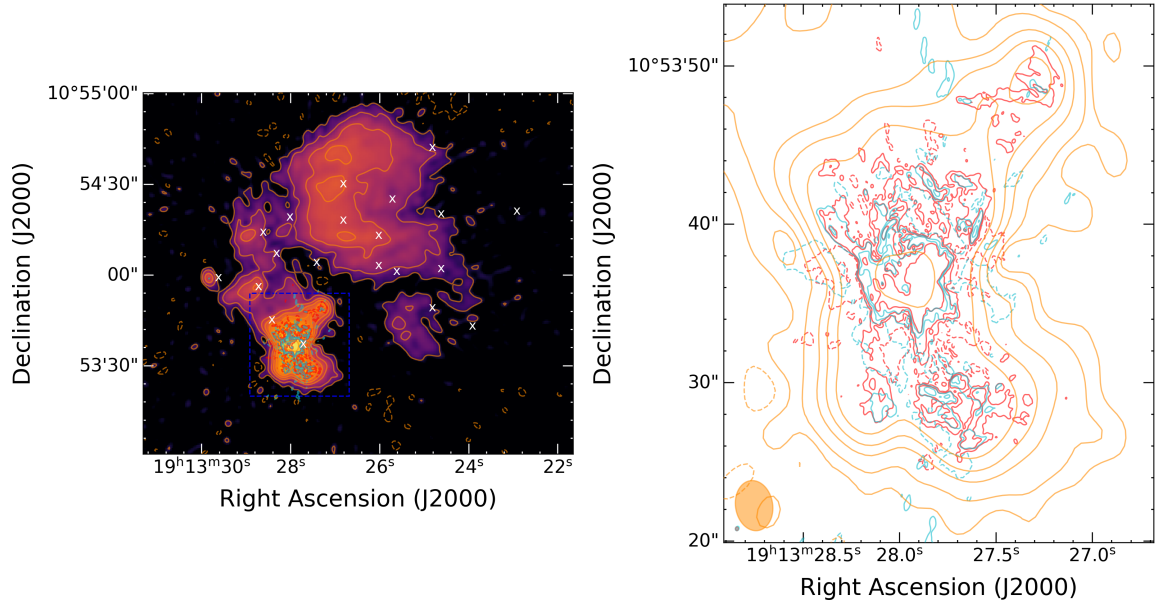


Figure 2. Left is L-band VLA (20 cm) continuum maps with VLA contours overlaid (1.3 cm–cyan, 6 cm–red, 20 cm–blue) of G45.12+0.13, with the synthesized beams shown in the lower corners. The white \times symbols are the location of the sources in the cluster reported by Vig et al. (2006). Notice the offset in the peak intensity position from the results of Vig et al. (2006) with respect to the VLA observations. Right is showing a zoom region of source S14 with the VLA contours of the three bands. The contour levels are at $[-5, 5, 20, 100] \times 35 \mu\text{Jy}/\text{beam}$ for C-band, at $[-5, 5, 15] \times 120 \mu\text{Jy}/\text{beam}$ for K-band and at $[-3, 3, 10, 30, 55, 100, 300, 500] \times 0.25 \text{ mJy}/\text{beam}$ for the L-band.

Table 14. Multiplicity in G35.58-0.03.

Source	R.A. (J2000)	Decl. (J2000)	Spectral Index	Association	New Detection
30A	18:56:22.52	+02.20.30.5	0.7(0.1)	IR	Yes ^a
30B	18:56:22.62	+02.20.34.7	<-1.1	...	Yes ^b
30C	18:56:22.57	+02.20.24.3	<-0.3	...	Yes ^b
30D	18:56:22.47	+02.20.24.8	<-1.2	...	Yes ^b
30E	18:56:22.55	+02.20.21.4	-0.5(0.1)	...	Yes ^b
30F	18:56:22.43	+02.20.20.5	<-0.5	...	Yes ^b
30G	18:56:22.39	+02.20.19.7	<-1.0	...	Yes ^b
30H	18:56:22.46	+02.20.18.9	<-1.9	...	Yes ^b
30J	18:56:22.19	+02.20.21.5	<0.6	...	Yes ^b
30K	18:56:22.19	+02.20.21.5	<0.1	...	Yes ^b
30N	18:56:22.53	+02.20.27.6	-0.5(0.4)	IR, mm	Yes ^c
30S	18:56:22.52	+02.20.27.2	0.2(0.1)	IR, mm	Yes ^c
31	18:56:22.62	+02.20.27.9	0.0(0.1)	MIR, mm	No

NOTE— Units of R.A. are hours, minutes, and seconds. Units of Decl. are degrees, arcminutes, and arcseconds.

^a These sources have been previously detected at different wavelengths but not in radio continuum.

^b These sources have been previously observed but not detected.

^c These sources have been previously detected in radio continuum but we are resolving into multiple detections.

G35.58-0.03 30 and 31: Sources 30 and 31 have previously been referred to as UC HII regions (e.g., Kurtz et al. 1994). For source 31, based on its morphology

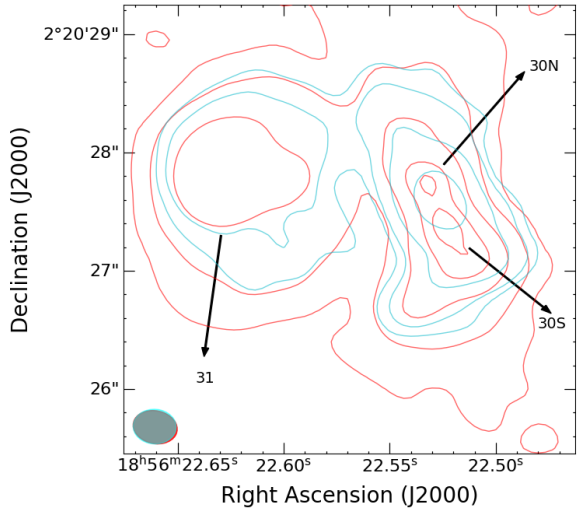


Figure 3. VLA continuum maps of the triple system towards G35.58-0.03 observed at 1.3 and 6 cm. The beam sizes are indicated in the lower left-hand corner. The contour levels are at $\sigma \times (-10, 10, 100, 500, 1200, 1700)$ for C-band (red) and $\sigma \times (-10, 10, 25, 100, 500)$ for K-band (cyan), with the σ value reported in Table 1

in the centimeter and its estimated spectral index, we agree with its nature being an UC HII region. Moreover, source 31 appears to have already a central protostar based on its association with a bright and compact MIR source (SOMA II).

To our knowledge, we are resolving for the first time source 30 into two components. Specifically, at the C-band (see Figure 3) source 30 appears slightly resolved into two sources, which we have labeled 30S and 30N and they appear to be slightly aligned in the NE-SW direction.

Their elongation, which appears aligned in the direction of the larger scale molecular outflow, and their association with water masers appears to suggest a scenario in which source 30S and 30N could be part of an ionized jet. However, we cannot be certain of this with the current observations. Moreover, source 30, which shows several tracers of ongoing star formation, appears to be in a younger evolutionary stage than source 31. Furthermore, the estimated spectral index of ~ 0.7 , derived from the inner scale encompassing Source 30, aligns with the typical values observed for ionized jets associated with young stellar objects (YSOs). (e.g., Reynolds (1986); Anglada et al. (1998); Tanaka et al. (2016))

G35.58-0.03 30A: Source 30 A appears in the MIR observations as two-pronged diffuse emission in the northern direction (SOMA II). We have detected, for the first time, associated centimeter emission with a bubble-like morphology.

G35.58-0.03 30B-30K: Sources 30B to 30K are presented in Figures 1 and 4. To our knowledge, these are new weak radio detections (for more details see Table 14). The majority of the sources are only detected at C band except for 30E that is detected at both C and K-band. Figure 4 is centered $\sim 2.2''$ to the SW of the SOMA scale (coordinates in Table 1).

These new sources present a variety of morphologies: mostly compact sources, but with some of them slightly extended. Upper limit estimates of the spectral indices indicate that all these new sources, except for 30J, are consistent with synchrotron emission. Given their slight alignment with the direction of the molecular outflow, these sources may be part of an ionized jet that is being driven by source 30, which is itself elongated in the same direction.

Despite our suggested classification of an ionized jet for source 30, defining an intermediate scale for this source is not feasible. The extent of the presumed jet is already enclosed within the SOMA scale, with the caveat that this scale contains the UCHII region in source 31 and the bubble-like morphology source 30A. Any intermediate scale would face the same issue; therefore, we omitted this scale for this particular case.

The high multiplicity observed in this region raises the question of whether these detections are real or artifacts. In general, we expect artifacts to exhibit symmetric properties, but, as shown in Figures 1, 3, and 4, we can see that this is not the case for most of our detections. Furthermore, based on estimates of calibration and deconvolution errors, we find that Source 30B is at least 25 times brighter than what would be expected for a Point Spread Functions (PSF) artifact. This implies that detections at least 10 times fainter than Source 30B could plausibly be artifacts. Among our sources, this criterion only applies to Source 30J, which is approximately 10 times fainter than 30B. Therefore, we conclude that most of our detections are likely real.

3.1.4. IRAS 16562-3959

IRAS 16562-3959, also known as G345.49+1.47, is a region located at 1.7 kpc and the massive core host of a massive star in an early stage of evolution (Guzmán et al. 2010). This region has been observed at multiple wavelengths, including centimeter continuum, mm, IR and X-ray (Guzmán et al. 2010, 2014, 2016, 2018; Liu et al. 2019; Montes et al. 2020).

Guzmán et al. (2011) reported a quadrupolar molecular outflow using CO(6-5) and CO(7-6) lines. This morphology is explained by the presence of two collimated bipolar outflows, one lying in the SE-NW direction related to the ionized jet detected by Guzmán et al. (2010),

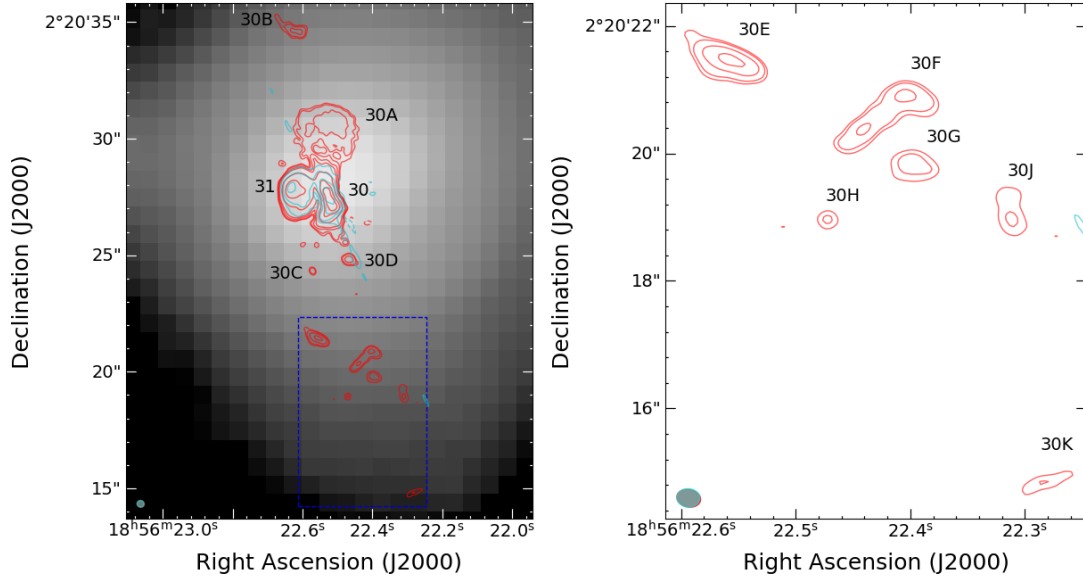


Figure 4. VLA continuum 1.3 and 6 cm maps showing the multiplicity of region G35.58-0.03 in the SW of the SOMA scale. The beam sizes are indicated in the lower left-hand corner. The contour levels are at $\sigma \times (-8, 8, 11, 20, 35)$ for C-band and $\sigma \times (-5, 5, 10)$ for K-band, with the σ value reported in Table 1

and another in the N–S direction that could be related to the unresolved millimeter source 13 in Guzmán et al. (2014).

Guzmán et al. (2016) reported nine radio detections at 5, 9, 17, and 19 GHz using ATCA observations. The central source has a counterpart at 3 mm and X-ray (source 10 at 3 mm and source 161 in X-ray) (Guzmán et al. 2014; Montes et al. 2020), and has also been detected in the MIR by the SOMA II study.

For our analysis we used ATCA images at 5, 9, 17 and 19 as presented by Guzmán et al. (2016). We focus on regions IRAS 16562-3959 and 16562-3959 N. With IRAS 16562-3959 N being a new region added to the sample in SOMA III, due to the detection of a point source in the IR maps, by the observations analyzed in SOMA II.

The SOMA scale in IRAS 16562-3959 (see Figure 1) includes only the main source (C), the two inner lobes (i.e., I-E and I-W) and the three additional sources (1 to 3) reported by Guzmán et al. (2016). So, for the purpose of this study, we only focus on the sources within the SOMA scale. In Table 15 we present more information about the multiplicity in IRAS 16562-3959 (within the SOMA scale) such as the R.A. and Decl. positions, the estimated spectral indices, association with other wavelengths, and whether or not the source is a newly reported radio detection.

Table 15. Multiplicity in IRAS 16562-3959.

Source	R.A. (J2000)	Decl. (J2000)	Spectral Index	Association	New Detection
C	16:59:41.61	−40:03:43.7	0.8(0.1)	Xray, IR, mm	No
I-E	16:59:41.93	−40:03:44.6	−0.6(0.1)	Xray, mm	No
I-W	16:59:41.32	−40:03:43.1	−0.6(0.1)	Xray, mm	No
1	16:59:42.42	−40:03:31.0	>1.5	...	No
2	16:59:42.86	−40:03:36.3	>1.9	Xray, IR, mm	No
3	16:59:41.67	−40:03:47.9	>3.3	...	No
4	16:59:40.77	−40:03:46.9	<1.3	...	Yes ^a

Table 15 continued

Table 15 (*continued*)

Source	R.A. (J2000)	Decl. (J2000)	Spectral Index	Association	New Detection
--------	--------------	---------------	----------------	-------------	---------------

NOTE— Units of R.A. are hours, minutes, and seconds. Units of Decl. are degrees, arcminutes, and arcseconds.

^a These sources have been detected in [Guzmán et al. \(2010\)](#), but were not reported. For completeness we include them following our criteria of 5σ detections.

IRAS 16562-3959: We find 7 radio sources within the SOMA scale. Detections C, I-E and I-W (following the nomenclature of [Guzmán et al. \(2010\)](#) and [Guzmán et al. \(2016\)](#)) were detected at all frequency bands. Meanwhile detections 1, 2 and 3 were only seen at the higher frequency bands (17.0 and 22.8 GHz) and a new detection, labeled as detection 4 (following the convention from [Guzmán et al. \(2016\)](#)), was found only at the lower frequency bands (5.5 and 9.0 GHz).

Detections C, 1-E and 1-W all show a compact morphology and using our own regions to measure the flux densities, we report an estimated spectral index of $\alpha \sim 0.8$ for detection C. This value is consistent with the spectral index reported by [Guzmán et al. \(2014\)](#) of 0.92 ± 0.01 at a wide frequency range of 1 to 100 GHz. Both our calculation and the previous reported values are in the range for typical ionized jets associated with YSOs (e.g., [Reynolds \(1986\)](#); [Anglada et al. \(1998\)](#); [Tanaka et al. \(2016\)](#)), and is consistent with the contemporaneous radio jet/HC HII region nature described in detail in [Guzmán et al. \(2016\)](#).

Detections 1-E and 1-W are considered lobes of the radio-jet in source C, and for both we report negative spectral indices which suggest non-thermal emission. The location of these two detections, the morphology and the optically thin free-free emission suggest that radio emission of the lobes comes from the synchrotron radiation that arises from the ionized radio jet. In contrast with [Guzmán et al. \(2016\)](#), we report some differences in the spectral index values due to the different regions used to measure the flux densities, but the non-thermal nature of the emission in the lobes remains.

Given the clear jet-like morphology we also measure the fluxes using an intermediate scale, as previously described, that encompass the central source (detection C) and the two radio lobes. From this scale we report a spectral index of $\alpha \sim 0.4$.

Sources 1, 2 and 3 present a compact morphology and we report lower limits in spectral index shown in Table 15. We have similar results to those of [Guzmán et al. \(2016\)](#) so arrive at the same conclusions in terms of the nature of the sources. [Guzmán et al. \(2016\)](#) explains the nature of these detections in Section 4.2.2 of their paper.

In summary, source 1 may be of extragalactic nature, source 2 is believed to be an HC HII region associated with a young high-mass star, and the free-free emission from source 3 comes from a low-mass YSO.

From our criteria and for full completeness we report all detections above a 5σ threshold. As a result of this, we report a new detection, source 4, that is only detected at C-band and shows a small elongation to the South (see Figure 1). We report an upper limit in the estimated spectral index shown in Table 15. This source can be clearly seen in Figure 7 of [Guzmán et al. \(2016\)](#), but they do not report this as a detection.

IRAS 16562-3959 N: In these observations we were not able to detect source IRAS 16562-3959 N which is a MIR source reported by [SOMA III](#) as a secondary region around IRAS 16562-3959. This point source was detected using IR data and, moreover, we see this new detection at the shortest wavelengths (MIR), but not in the longest wavelengths (FIR) of the observations analyzed in [SOMA II](#).

3.1.5. *G305.20+0.21*

The G305.2+0.2 complex is a vast high-mass star-forming region located at a distance of 4.1 kpc ([Krishnan et al. 2017](#)) in the southern Galactic Plane. Within the region, there are two locations separated by $22''$ named G305A (G305.21+0.21) and G305B (G305.20+0.21) where Class II methanol (CH_3OH) masers have been detected ([Norris et al. 1993](#); [Walsh & Burton 2006](#); [Walsh et al. 2007](#)). Additionally, G305C has been recently reported by [SOMA II](#) as an IR source located at $14''$ to the east of G305B, and it is detected at all SOFIA wavelengths showing NIR counterparts, as well.

From previous radio continuum observations toward G305.20+0.21 there are reports of two detections, which are prominent extended HII regions labeled as G305HII(SE) and G305HII by [Walsh et al. \(2007\)](#). These regions are located about $30''$ to the southeast of G305A and $15''$ to the southwest of G305B, respectively ([Walsh et al. 2007](#); [Phillips et al. 1998](#)).

Figure 1 show the observations toward this region, where the centimeter data images were made using a minimum baseline length of 1.5 km. The main reason for doing this was to improve the detections of the compact radio emission associated with G305A and G305B,

which are our sources of interest, by filtering out the bright, extended emission from the two HII regions (i.e., G305HII(SE) and G305HII) located to the south of each of them.

G305A (G305.21+0.21): This source is prominent at MIR and FIR (SOMA II) and has been observed at 8.6 and 18 GHz, but no radio detections have been reported at sensitivity levels of 0.9 mJy and 0.22 mJy, respectively (Phillips et al. 1998; Walsh et al. 2007). With our ATCA observations at 5.5, 9, 17 and 22.8 GHz, we report a single detection within the region G305A that we label as G305A ATCA-1 (see Figure 1: G305.21+0.21 (G305A)). This source coincides with the methanol maser reported by Walsh & Burton (2006) and shows a slight elongation at the lower frequencies.

For G305A we report an estimated spectral index of $\alpha \sim 0.3$, a result that indicates thermal emission. SOMA II suggested that G305A is a much younger and more embedded source than G305B and in a hot core phase, rich in molecular tracers (Walsh et al. 2007).

G305B (G305.20+0.21): Region G305B is the brightest MIR source associated with the methanol masers. However, no radio emission has been previously detected towards this region (Walsh et al. 2007). In our ATCA observations (see Figure 1) we report 4 sources labeled G305B ATCA-1, G305B ATCA-2, G305B ATCA-3 and G305B ATCA-4 (hereafter sources 1, 2, 3 and 4). In Table 16 we present more information about the multiplicity in G305B such as the R.A. and Decl. positions, the estimated spectral index, association with other wavelengths, and whether this source is a new radio detection or not.

Table 16. Multiplicity in G305.20+0.21 (G305B)

Source	R.A. (J2000)	Decl. (J2000)	Spectral Index	Association	New Detection
G305B ATCA-1	13:11:10.56	-62.34.38.3	-0.7(0.2)	IR	Yes ^a
G305B ATCA-2	13:11:10.04	-62.34.40.1	-0.8(0.2)	...	Yes ^b
G305B ATCA-3	13:11:09.63	-62.34.38.7	-0.6(0.2)	...	Yes ^b
G305B ATCA-4	13:11:10.99	-62.34.37.8	<-1.7	...	Yes ^b

NOTE—Units of R.A. are hours, minutes, and seconds. Units of Decl. are degrees, arcminutes, and arcseconds.

^a These sources have been previously detected at different wavelengths but not in radio continuum.

^b These sources have been observed but not detected.

Source 1 is the main detection in the region, and in our ATCA observations, this source is seen at all frequencies (5.5, 9, 17 and 22.8 GHz) and exhibits a morphology with a slight elongation in the NE-SW direction. SOMA II was able to resolve this source into two sources (G305B1 and G305B2) using high-spatial-resolution *Gemini* observations, finding morphologies that are also aligned in the NE-SW direction. They suggested that both sources are part of an outflow cavity. Our spectral index estimates show that the ionized material associated with this region is of non-thermal nature, suggesting the existence of a very fast jet in the region.

To our knowledge, sources 2, 3 and 4 are also new detections in the radio continuum. Source 2 is seen in all our ATCA observations and, similarly to source 1, shows a slight elongation in the NE direction and exhibits a spectral index that indicates non-thermal emission.

Source 4 is a faint compact eastern source only seen at the lowest frequencies (5.5 and 9 GHz), and we report a limit on its spectral index (see Table 16). On the other hand, source 3 is seen at all frequencies and presents an elongated morphology in the SE-NW direction that appears as a double peak at the longest contour levels shown in Figure 1. This source may be part of the HII region in Walsh et al. (1999), but in our observations we report it as an independent source. We report a negative spectral index ($\alpha \sim -0.6$) suggesting non-thermal emission.

Since sources 1, 2, and 4 are aligned in the same SW-NW direction, exhibit relatively compact morphologies and negative spectral indices, we conclude that the most likely nature of these independent sources is that they are knots from a non-thermal jet. Following our convention for sources with jet-like morphology, we measured the flux densities at an intermediate scale that encompasses the central source and the jet knots (Sources 1, 2, and 4). At this scale, we estimate an upper limit on

the spectral index of $\alpha < -1.2$, which is indicative of a non-thermal jet in the region.

Additionally, source G305C is within the SOMA scale for region G305B, but we are not detecting any radio source at our sensitivities levels. It is important to highlight that due to the minimum baseline length used in our images toward these regions, the flux measured for the SOMA scale corresponds to a lower limit, specially for source G305B due to the proximity to the HII region which has been filtered out in our images.

3.1.6. G49.27-0.34

G49.27-0.34 is a protostar located in an Infrared Dark Cloud (IRDC) at a kinematic distance of 5.55 kpc (Cyganowski et al. 2009). To date no molecular outflow has been detected towards this region. Two Class I 44 GHz CH₃OH masers spots have been detected in this region while no 6.7 GHz CH₃OH, 25 GHz CH₃OH or thermal masers have been detected (Cyganowski et al. 2009; Towner et al. 2017).

In our 1.3 and 6 cm observations we report 5 detections within the SOMA scale. Table 17 shows some information about the multiplicity in G49.27-0.34, i.e., the coordinates, estimate spectral index, association at other wavelengths, and whether or not a source is a new radio detection. We discuss each detection below.

Table 17. Multiplicity in G49.27-0.34.

Source	R.A (J2000)	Decl. (J2000)	Spectral Index	Association	New Detection
CM1	19:23:06.87	+14.20.17.3	0.8(0.1)	IR	No
CM2A	19:23:06.66	+14.20.11.6	1.6(0.2)	IR	Yes ^a
CM2B	19:23:06.62	+14.20.12.1	> 0.7	IR	Yes ^a
CM2C	19:23:06.58	+14.20.11.9	0.0(0.1)	IR	Yes ^a
CM3	19:23:06.71	+14.19.59.0	< 0.5	IR	Yes ^b

NOTE— Units of R.A. are hours, minutes, and seconds. Units of Decl. are degrees, arcminutes, and arcseconds.

^a These sources have been previously detected in radio continuum but we are resolving into multiple detections.

^b These sources have been previously detected at different wavelengths but not in radio continuum.

CM1: Source CM1 is an extended source previously seen at 1.3, 3.6 and 20 cm (Towner et al. 2017; Cyganowski et al. 2011; Mehringer 1994) and it is coincident with MIPS 24 μ m emission (Carey et al. 2009). There are no reports of association with Class I 44 GHz CH₃OH masers.

Cyganowski et al. (2011) suggests that CM1 is a single ionizing star of spectral type B0V based on optically thin free-free emission and the ionizing photon flux. Our 1.3 cm flux density values are one order of magnitude less than that reported by Cyganowski et al. (2011); Towner et al. (2017) with VLA observations and resolutions of $\sim 0.8''$ (2.63 and 1.62 mJy). This difference is likely due to the different resolutions.

CM2: The MIR peak observed in SOMA II is associated with source CM2, previously reported as an unresolved, 4σ detection at 0.027 mJy/beam rms at 3.6 cm (Cyganowski et al. 2011). Additionally, Cyganowski et al. (2011) estimated a spectral index limit of <0.2

at a resolution of $\sim 0.9''$. Using our VLA data, we are able to resolve source CM2 into three components, which we have labeled as CM2A, CM2B and CM2C, with all sources detected at both 1.3 and 6 cm observations.

CM2A is the central and brightest source at 1.3 cm among the components of CM2. It shows a compact morphology and a very steep spectral index of 1.6.

CM2B is detected as an unresolved source, located $\sim 0.7''$ SW of the central component (CM2A) and it is the weakest detection in this system. We estimated a lower limit for the spectral index of 0.7.

CM2C is located about $1.2''$ of the central component in the same direction as CM2B. It presents a compact morphology with a flat spectral index suggesting thin free-free emission.

Given the extended morphology of the CM2A-CM2C sources at low frequencies, we also measure the flux densities using an intermediate scale that incorporates the three components. The estimated spectral index at this scale yields a value of 0.7, given an indication that CM2

could be a radio jet with CM2A being the driven source of this jet.

CM3: From the contour maps in Cyganowski et al. (2011); Towner et al. (2017), source CM3 shows MIPS 24 μm emission and SOMA II also detected this source in the SOFIA IR maps, but not in the NIR. This source has no previous radio detections at 1.3 and 3.6 cm. In our observations we are able to detect this source, but only at 6 cm (C-band).

CM3 exhibits a compact morphology and we report a relative flat spectral index with an upper limit of 0.5, indicative of thermal emission. To our knowledge, we are detecting this source for the first time in radio frequencies and its naming follows the convention of the main region, G49.27-0.34.

3.1.7. G339.88-1.26

G339.88-1.26 (or IRAS 16484-4603) is a massive protostar located at 2.1 kpc (Krishnan et al. 2015), that has been previously observed at a variety of wavelengths. De Buizer et al. (2002) resolved the central MIR emission into three peaks (1A, 1B and 1C) and radio continuum observations have identified the central source is associated with a radio jet and the other two sources are associated with radio outflow lobes (Ellingsen et al. 1996; Purser et al. 2016), label as C, NE and SW. Using ALMA data, Zhang et al. (2019b) reported two molecular outflows towards this region positioned at the source C. One of this outflows is located in the northeast-southwest orientation and exhibits the same angle as the ionized outflow reported by Purser et al. (2016).

With 19.7 μm SOFIA data, both molecular outflows are detected; however, at longer wavelengths, only the molecular outflow associated with the ionized outflow is observed. SOMA II suggests this could be due to extinction, and that the detection of red and blue shifted emission on both sides suggests a near side-on view of the outflows.

For our analysis we used S. Purser’s ATCA observations at 5.5, 9.0, 17.0, and 22.8 GHz from Purser et al. (2016). In our analysis we consider the same three sources NE, C, and SW reported by Purser et al. (2016).

Source C presents a compact morphology at higher frequencies, but shows a slight extension at the lower frequencies, particularly at 5.5 GHz. We report a spectral index of $\alpha \sim 0.9$. Meanwhile, sources NE and SW have spectral indices of $\alpha \sim -0.4$ and $\alpha \sim -0.8$, respectively. Both sources exhibit relatively compact morphologies, especially source SW.

As mentioned by Purser et al. (2016), source G339.88-1.26 shows characteristics consistent with an ionized radio jet driven by the central source C and two lobes of

non-thermal emission. Given this jet-like morphology of the region we also measure the flux densities using an intermediate scale that encompass the three sources. We report a spectral index of $\alpha \sim -0.1$ for the intermediate scale suggesting that the non-thermal emission from the lobes is more prevalent at this scale.

3.2. Radio SEDs

In Figure 5 we present the E-SEDs, i.e., radio + IR SEDs, for our nine protostellar sources. The dashed lines correspond to the best fit to the data using a power law of the form $S_\nu \propto \nu^\alpha$, where α is the spectral index at the various scales: “SOMA”; “Intermediate”; and “Inner”, as described above. The spectral index was calculated using the flux density at the central frequencies from the images, so α is calculated over a wide frequency range (>20 GHz). The uncertainty in the spectral index was calculated with a Monte Carlo simulation that bootstrapped the flux density uncertainties. We estimated an upper limit in the spectral index for non-detections at higher frequencies using a value of S_ν of 3σ .

It is important to mention that at higher frequencies the free-free emission is likely contaminated by dust emission (see Brogan et al. (2016)), therefore adding some additional systematic uncertainty to the measurement of the free-free fluxes.

4. ANALYSIS AND DISCUSSION

The main goal of this paper is to analyze the morphology, multiplicity, and the estimated spectral indices of the sources of the SOMA II sample to better understand the nature of the sources using radio observations at different frequencies. Our sample consists of regions located at distances greater than 1 kpc, with some exhibiting low radio flux densities (<3 mJy), such as G305.20+0.21 (G305B), G305.21+0.21 (G305A), G49.27-0.34, and G339.88-1.26. In contrast to SOMA Radio I, seven of the eight sources analyzed showed relatively low radio flux densities.

With the available data, we aim to assess the nature of the sources based on their morphology and spectral index. For sources that have been previously analyzed, we refer to past studies that have characterized their nature and compare our results, specifically in terms of morphology and spectral index (see §3.1). This comparison allows us to refine our understanding of the radio emission mechanisms associated with each source.

4.1. Multiplicity and new detections

Most of the sources analyzed in this paper present a high level of multiplicity, except for G305A which only has one detection within the SOMA scale. Furthermore,

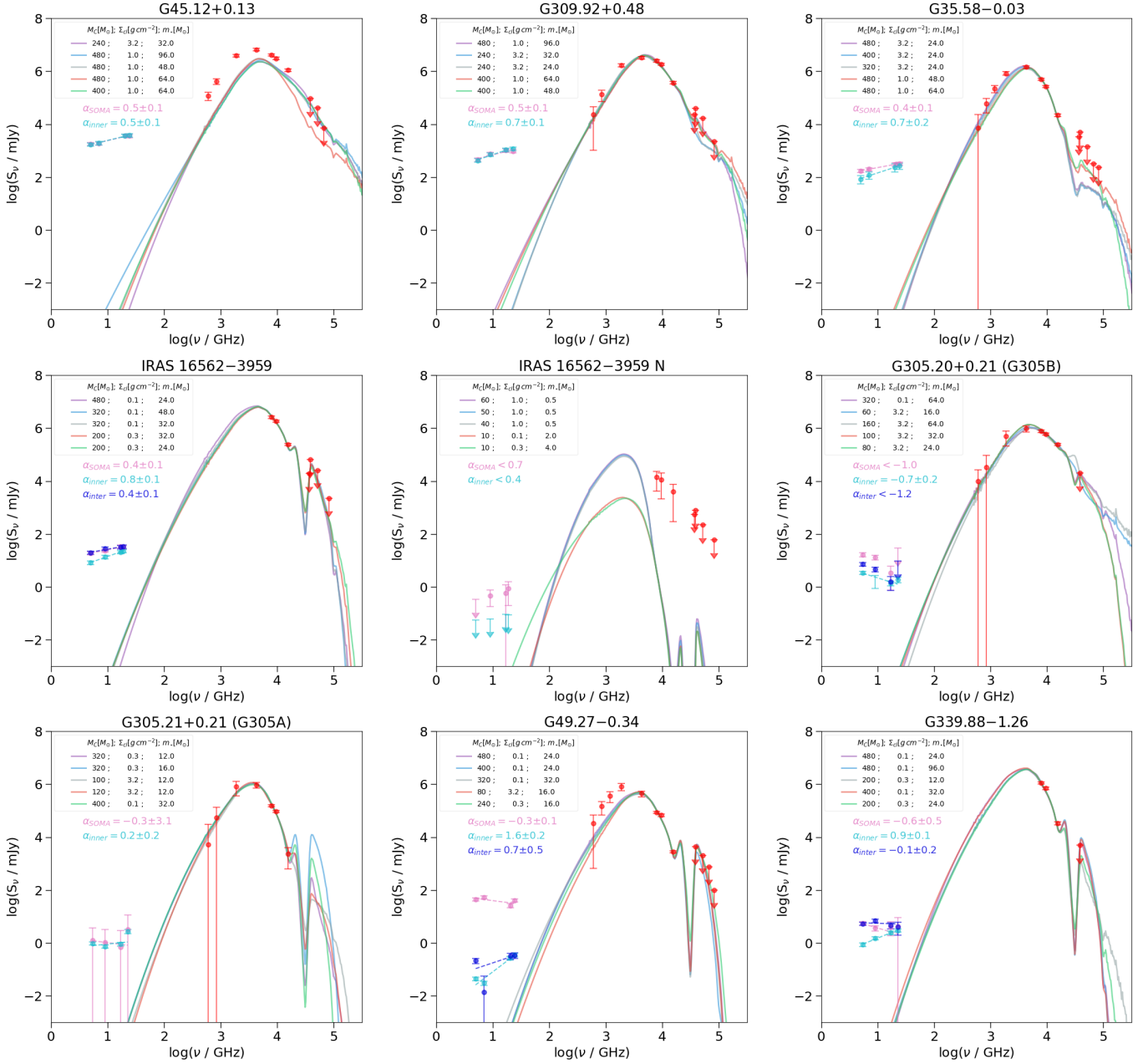


Figure 5. Extended spectral energy distributions (E-SEDs) of SOMA protostars, consisting of radio and IR SEDs. The circles correspond to the flux density as a function of the frequency at each scale (magenta: *SOMA*; blue: *Intermediate*; cyan: *Inner*). Error bars are explained in §3.2. The solid lines show the five best fits (see legend) to the IR data SED from the Zhang & Tan (2018) models as fit by *SOMA IV* (see Appendix in *SOMA IV*), and the dashed lines are the best fit of the radio data using a power law of the form $S_\nu \propto \nu^\alpha$.

no source has been detected in IRAS 16562 N at the sensitivity level ($\sim 21 \mu\text{Jy} - 28 \mu\text{Jy}$) of the analyzed ATCA data.

Across our 9 target regions, we detected a total of 37 sources. See §3.1 for individual analysis of each source. About 38% of the sources are new detections, hence in §3.1 we made the notation of two types of new detections: (A) sources that have been previously observed

and detected at different wavelengths, but not at radio frequencies; and (B) sources that have never been detected at any wavelength. This type of new detection could be regions that have been observed at radio but remained undetected due to limitations of sensitivity or possible variable sources. Detections of regions in which we present the first radio observations also fall in this category.

Table 18. Parameters from Radio Continuum at the sensitivity limit at 5 GHz.

Region	$\log N'_{\text{Ly}}$ ^a	Sp ^b	M_{\odot} ^c
G45.12+0.13	45.34	B1	11.8
G309.92+0.48	46.03	B0.5	14.8
G35.58-0.03	45.49	B1	11.8
IRAS 16562-3959	43.38	B3	5.4
IRAS 16562-3959 N	43.40	B3	5.4
G305.20+0.21	44.98	B1	11.8
G305.20+0.21 A	44.96	B1	11.8
G49.27-0.34	44.07	B3	5.4
G339.88-1.26	44.01	B3	5.4

NOTE—

^a Values calculated using equations from Kurtz et al. (1994); Panagia & Walmsley (1978).^b Spectral type estimation made from table II in Panagia (1973).^c The estimate of the mass was taken from Pecaut & Mamajek (2013)

Of the 37 sources, we report 13 new detections (9 in G35.58-0.03, 1 in IRAS 16562-3959, and 3 in G305B or G305.20+0.2) classified as Type B detections, which, to the best of our knowledge, have never been detected at any wavelength.

To make sure we are not missing any UCHII regions, we estimate the physical properties from the 5 GHz sensitivity limit (rms) using equation 1 and 3 from Kurtz et al. (1994) and equation A.2.3 from Panagia & Walmsley (1978). These equations assume spherical symmetry and optically thin emission from a uniform-density plasma with $T_e = 10^4$ K. The results are listed in Table 18, where column 1 is the region name, column 2 is the logarithm of the Lyman continuum flux ($\log N'_{\text{Ly}}$) required for ionization. With the $\log N'_{\text{Ly}}$ and the results from Table II in Panagia (1973), we estimate the spectral type of the ionizing star (listed in column 3), further assuming that a single ZAMS star is photoionizing the nebula and producing the Lyman continuum flux. The distances used for these calculations are listed in Table 1. Column 4 is the estimate mass of the spectral type of the ionizing star from Pecaut & Mamajek (2013).

The results from Table 18 give us an estimation of the lowest mass ZAMS star that we can detect with our current observations. This serves as completeness parameter on the multiplicity at the different regions, especially for region IRAS 16562-3959 N where we do not report any detections and in this case the completeness level goes down to around $5.4 M_{\odot}$.

4.2. Nature of the sources

By using previous studies on these sources, as well as results from our radio observations, we have assessed the nature of each individual source (see §3.1). From a sample point of view of the SOMA II sources, out of the 37 detections it is important to mention that three of them are well defined radio jets given their morphology and the estimated spectral index. For example, IRAS 16562-3959 and G339.88-1.26, are both very well previously studied ionized jets. Both have a central source that exhibits a jet-like morphology and a spectral index in the range for typical ionized jets associated with YSOs (Reynolds 1986; Anglada et al. 1998; Tanaka et al. 2016), along with two additional sources classified as lobes that display non-thermal emission due to the synchrotron radiation. For G49.27-0.34 CM2A we report a spectral index in the typical range of ionized jets and two additional sources relatively close to the driving jet (CM2B at $0.7''$ and CM2C at $1.2''$), but both companions exhibit thermal emission.

We also propose a radio jet scenario for sources G35.58-0.03 and G305.20+0.21, based on the observed extended morphology, association with extended molecular outflows and evidence of knots from a non-thermal jet in the direction of the elongation. However, this classification remains less certain compared to other radio jets in the sample, and additional observations are needed to fully resolve and confirm the presence of the proposed non-thermal jets.

Additionally, we have three UC HII regions (G45.12+0.13 S14, G309.92+0.48 ATCA 1, and G35.58-0.03 31), following the suggestion of previous authors and the morphology of our detections and the reported spectral indices. The remaining sources are point sources being companion sources from the central detection or sources of an unknown nature, that could be of extragalactic nature or lower-mass YSOs. Most of them display a flat or negative spectral index suggesting non-thermal emission.

In terms of multiplicity, we find results similar to SOMA Radio I, where the analyzed regions exhibit high multiplicity, with multiple sources detected within the SOMA scale. In SOMA Radio I, seven out of eight regions showed at least two detections. In our sample, seven out of nine regions also show more than one detection, with G305.21+0.21 (G305A) having a single detection and IRAS 16562-3959 N showing no detections, likely due to our sensitivity limit.

In SOMA Radio I, we reported different evolutionary stages and nature of the sample, which included radio jets, HII regions, and variable stars. Four of the seven sources in that initial sample exhibited characteristics

consistent with radio jets, such as elongation in the same direction as the associated molecular outflow with a central ionized jet and knots in aligned detections. In the sample presented in this paper, we observe a similar distribution: five of the nine regions show evidence of hosting a radio jet on the SOMA scale. Of these five, three (IRAS 16562-3959, G49.27-0.34, G339.88-1.26) display well-defined jets with knots, while the remaining two (G305B: G305.20+0.21 and G35.58-0.03) are proposed as jet candidates based on characteristics discussed in detail in Section 3, including spectral index, morphology, and multiplicity. Additionally, source G45.12+0.13, has been previously reported to be associated with an UCHII region which is consistent with our assessment from Figure 6 (see below). Furthermore, this source shows ionized emission at the lowest frequency (L-band) that resembles an hour-glass morphology similar to the very massive protostar G45.47+0.05 which is also associated with an UC HII region that is driving a powerful photoionized outflow and a jet candidate (Zhang et al. 2019a).

4.3. The Radio - Bolometric Luminosity Relation

Here we expand on the analysis of the SOMA sample from the results presented in SOMA Radio I, who presented results for an initial sample of eight massive protostars. We add in the nine protostars selected from the seven high-luminosity regions analyzed in this paper.

Similar to Figure 3 in SOMA Radio I, in Figure 6 we present radio luminosity at 5 GHz from the Inner (left panel) and SOMA (right panel) scales versus bolometric luminosity. Note, when necessary, radio fluxes at $\nu = 5$ GHz have been estimated by scaling from adjacent frequencies using the derived spectral index. For the bolometric luminosity of SOMA sources (detections from SOMA I and II samples are squares and circles, respectively) we report the average of the “good” models from Table C1 of SOMA V and the error bar corresponds to the dispersion of these good models. We also show data for lower-mass YSOs associated with ionized jets from Anglada (1995) (small yellow dots). We scaled their fluxes from 3.6 cm, using a factor of 0.74, assuming that these sources have a spectral index $\alpha = 0.6$, which is the expected value of ionized jets. A power-law fit to these data of $(S_\nu d^2 / [\text{mJy kpc}^2]) = 8 \times 10^{-3} (L_{\text{bol}} / L_\odot)^{0.6}$ is shown with a dashed line. UC/HC HII regions from Kurtz et al. (1994) are represented with a \times symbols. Note, the bolometric luminosities of the low-mass YSOs and the UC/HC HII regions are not measured in exactly the same way as the SED-fitting method of the SOMA sources, for which we are reporting intrinsic bolometric luminosities of the fitted SED models. A plot show

the results based on isotropic bolometric luminosities is presented in Appendix A.

We examine several theoretical models for the radio luminosity of massive protostars and show these in Figure 6. The black dotted line is the radio emission expected from an optically thin HII region, given the Lyman continuum luminosity of a single zero age main sequence (ZAMS) star at a given bolometric luminosity (Thompson 1984). The light blue lines corresponds to the expected radio emission that arises from photoionization from a massive protostar forming via TCA, as predicted by the TTZ16 model, also for optically thin conditions at 5 GHz. These models have an initial core mass of $M_c = 60 M_\odot$ and the three cases correspond to clump environment mass surface densities of $\Sigma_{\text{cl}} = 0.316, 1$ and 3.16 g cm^{-2} . The lower mass surface densities correspond to lower accretion rates, for which protostellar contraction towards the ZAMS occurs sooner, i.e., at lower masses and lower values of L_{bol} . Note, these models do not include any contribution from shock ionization.

A model for estimating the radio emission from free-free emission from ionized gas produced by collisional ionization in shocks has been developed for a massive protostar forming from a $60 M_\odot$ core in a 1 g cm^{-2} clump environment by Gardiner et al. (2024). This radio emission is also shown in Figure 6 with dark blue lines. We note that the contribution from shock ionization is quite spatially extended, with the emission from a 25,000 au radius aperture (more closely matching the SOMA scale) being about a factor of 10 higher than that from a 1,000 au aperture (more closely matching the inner scale).

Comparing the distribution of SOMA Radio sources with the models, we note the following points. The SOMA Radio II sample, mostly being protostars of relatively high luminosity, help to better define the radio versus bolometric luminosity relation over the range from $L_{\text{bol}} \sim 10^4$ to $10^6 L_\odot$, which is a regime where it is rising rapidly. We find that the radio luminosity measured on the SOMA scale rises steeply by about five dex as bolometric luminosity increases by 1 dex. Such a steep rise is consistent with basic expectations of TCA massive protostar models.

Nevertheless, overall from the SOMA protostar sample we see that sources have relatively faint radio luminosities compared to predictions of protostellar models. This suggests that the rise in ionizing luminosity may occur only at relatively higher protostellar masses and luminosities. Such a relatively late rise in ionizing luminosity could be due to higher protostellar accretion rates or reflect systematic errors in the current proto-

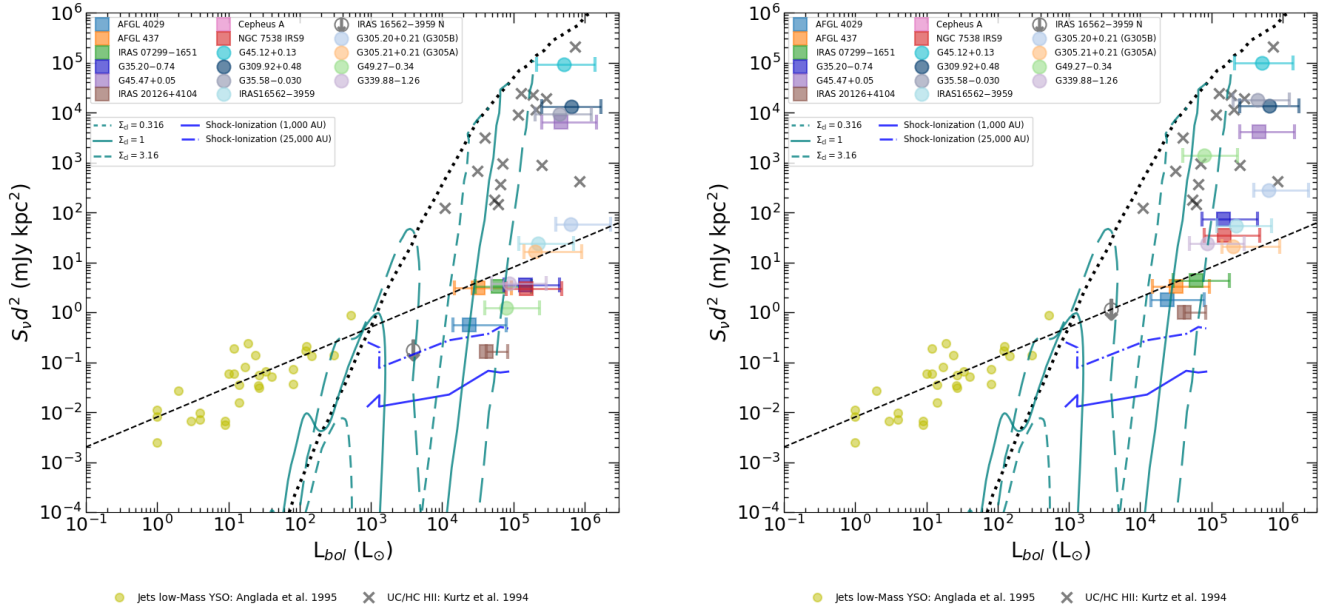


Figure 6. Radio luminosity at 5 GHz for the Inner scale (left) and for the SOMA scale (right) as a function of the bolometric luminosity of for 15 SOMA sources from SOMA Radio I (squares) and II (circles) (see legend). In each panel we also show lower-mass YSOs from [Anglada \(1995\)](#) (small yellow circles). The dashed line shows a power-law fit to these lower-mass YSOs ([Anglada et al. 2015](#)): $(S_\nu d^2 / [\text{mJy kpc}^2]) = 8 \times 10^{-3} (L_{bol} / L_\odot)^{0.6}$. The \times symbols are HC and UC HII regions from [Kurtz et al. \(1994\)](#). The black dotted line shows the radio emission expected from optically thin HII regions powered by ZAMS stars ([Thompson 1984](#)). The light blue lines show models for HII regions powered by TCA model protostars ([Tanaka et al. 2016](#)) (with $M_c = 60 M_\odot$ and $\Sigma_{cl} = 0.316, 1$ and 3.16 g cm^{-2} , as labeled). Note that these models, which do account for radiative transfer effects of the free-free emission, assume all of the ionizing photons are reprocessed by the HII region, i.e., with zero escape fraction. The dark blue lines show radio emission from shock ionization in simulations of a fiducial TCA protostar, i.e., forming from a $60 M_\odot$ core in a 1 g cm^{-2} clump environment ([Gardiner et al. 2024](#)), with the solid and dot-dashed lines showing emission from within 1,000 and 25,000 au of the protostar, respectively.

stellar models and their HII region radio emission (e.g., assumption all stellar EUV photons contribute to ionization / neglect of dust absorption). In addition, we caution that, at least on the SOMA scale, there is the possibility that we are missing radio flux due to interferometric filtering. A comparison with additional sets of theoretical models based on optically thin radio emission from the ionizing photon output of the TCA protostellar evolution models of [Zhang & Tan \(2018\)](#) is shown in Appendix B.

We note that the HC/UC HII region sample of [Kurtz et al. \(1994\)](#) does include sources with higher radio luminosities, potentially indicating a systematic change arising from source evolution from the protostellar phase or else reflecting biases in sample selection from a single intrinsic protostellar population that has inherent large variation in radio luminosity.

We see that the shock ionization model of [Gardiner et al. \(2024\)](#), which falls below the extrapolated lower-mass YSO relation, is consistent with the fainter end of the SOMA sample. Extending the comparison of the

models with SOMA data on intermediate-mass protostars is a major goal of the SOMA Radio III paper (in prep.).

5. SUMMARY AND CONCLUSIONS

We have presented results from radio continuum VLA and ATCA follow-up observations of massive protostars of the SOMA II sample following the framework developed in [SOMA Radio I](#). These radio observations help to give a precise localization of the protostar, allow a search for multiplicity, and trace the presence of ionized gas, which helps trace outflow morphology, especially via orientation of radio jet axes, and is expected to be a useful evolutionary indicator of massive protostars, especially as they approach the zero age main sequence when the contribution from photoionization is predicted to increase dramatically.

A summary of main finds is as follows. We have detected and analyzed emission from 8 out of the 9 massive protostars (from 7 primary regions), with the non-detection being related to IRAS 16562-3959 N, which

is an intermediate-mass protostar that is a secondary source in this region. Similar to SOMA Radio I regions, we have found a high level of “multiplicity” with 37 detections in the 7 regions. However, we caution that many of these sources are likely to be ionized gas jet knots, rather than independent stellar sources. Higher sensitivity observations are needed to better probe the presence of lower-mass YSOs that may be in the vicinity.

Given that the 7 primary protostars of the SOMA II sample were selected as being relatively high bolometric luminosity protostars, these data help to better define the radio - bolometric luminosity relation in this regime, i.e., from $\sim 10^4$ to $10^6 L_{\odot}$. We find that the radio luminosity, i.e., at 5 GHz, rises steeply by about five dex as bolometric luminosity increases by 1 dex. However, the caveat of the possibility of missing flux from extended ionized gas features needs to be kept in mind.

Many of our fainter radio sources have radio luminosities that are consistent with a simple power law extrapolation from a lower-mass YSO sample (Anglada 1995). However, this radio flux is about ten times higher than a theoretical model of radio emission from shock ionization of a fiducial TCA massive protostar (Gardiner et al. 2024). Nevertheless, shock ionization appears to be the most likely explanation for many of these sources, especially given the morphology of extended jet knots, while a contribution from photoionization, especially at the Inner scale, cannot be excluded. However, in the high radio luminosity regime, photoionization is expected to be dominant. Overall, these data are important for constraining theoretical models of massive protostar ionization and how this links to protostellar structure and evolutionary state.

6. ACKNOWLEDGMENTS

F. S. M. acknowledges support from the NRAO NINE (National and International Non-traditional Ex-

change) program. V. R. acknowledges support from NSF grant AST-2206437. J.C.T. acknowledges support from NSF grant AST-2206437 and ERC Advanced Grant 788829 (MSTAR). R.F. acknowledges support from the grants PID2023-146295NB-I00, and from the Severo Ochoa grant CEX2021-001131-S funded by MCIN/AEI/ 10.13039/501100011033 and by “European Union NextGenerationEU/PRTR”. The National Radio Astronomy Observatory and Green Bank Observatory are facilities of the U.S. National Science Foundation operated under cooperative agreement by Associated Universities, Inc. We acknowledge Simon Purser and Andres Guzmán for providing the ATCA images for sources G339.88-1.26 and IRAS 16562-3959, respectively.

Facility: VLA, ATCA

Software: CASA (McMullin et al. 2007), Astropy (Astropy Collaboration et al. 2013, 2018), APLpy (Robitaille & Bressert 2012; Robitaille 2019)

7. ORCID IDS

F. Sequeira-Murillo

<https://orcid.org/0000-0001-8169-1437>

V. Rosero <https://orcid.org/0000-0001-8596-1756>

J. Marvil <https://orcid.org/0000-0003-1111-8066>

J. C. Tan <https://orcid.org/0000-0002-3389-9142>

R. Fedriani <https://orcid.org/0000-0003-4040-4934>

Y. Zhang <https://orcid.org/0000-0001-7511-0034>

A. Robinson <https://orcid.org/0009-0007-4080-9807>

P. Gorai <https://orcid.org/0000-0003-1602-6849>

K. E. I. Tanaka <https://orcid.org/0000-0002-6907-0926>

M. Liu <https://orcid.org/0000-0001-6159-2394>

J. M. De Buizer <https://orcid.org/0000-0001-7378-4430>

M. T. Beltran <https://orcid.org/0000-0003-3315-5626>

R. D. Boyden <https://orcid.org/0000-0001-9857-1853>

APPENDIX

A. RADIO LUMINOSITY VERSUS ISOTROPIC BOLOMETRIC LUMINOSITY

Figure A1 shows a similar plot to Figure 6, but in this case we used the average of the good models of the isotropic bolometric luminosity (Table C.1 of SOMA V). Everything else is the same as Figure 6.

B. EVOLUTIONARY TRACKS FROM RADIO LUMINOSITIES

Figure B1 makes a comparison of the SOMA Radio data at the inner (top) and SOMA (bottom) scale, with the full set of protostellar evolutionary tracks from Zhang & Tan (2018), i.e., with $M_c = 10, 30, 60, 120, 240$ and $480 M_{\odot}$ with $\Sigma_{cl} = 0.316 \text{ g cm}^{-2}$ (left), 1 g cm^{-2} (center) and 3.16 g cm^{-2} (right). In these models the radio luminosities are not set from radiation transfer like the tracks from (Tanaka et al. 2016), but instead assumes a simple spherical HII region. Meanwhile, Figure B2 shows the same information but with the average of the good models of the isotropic bolometric luminosity (Table C.1 of SOMA V).

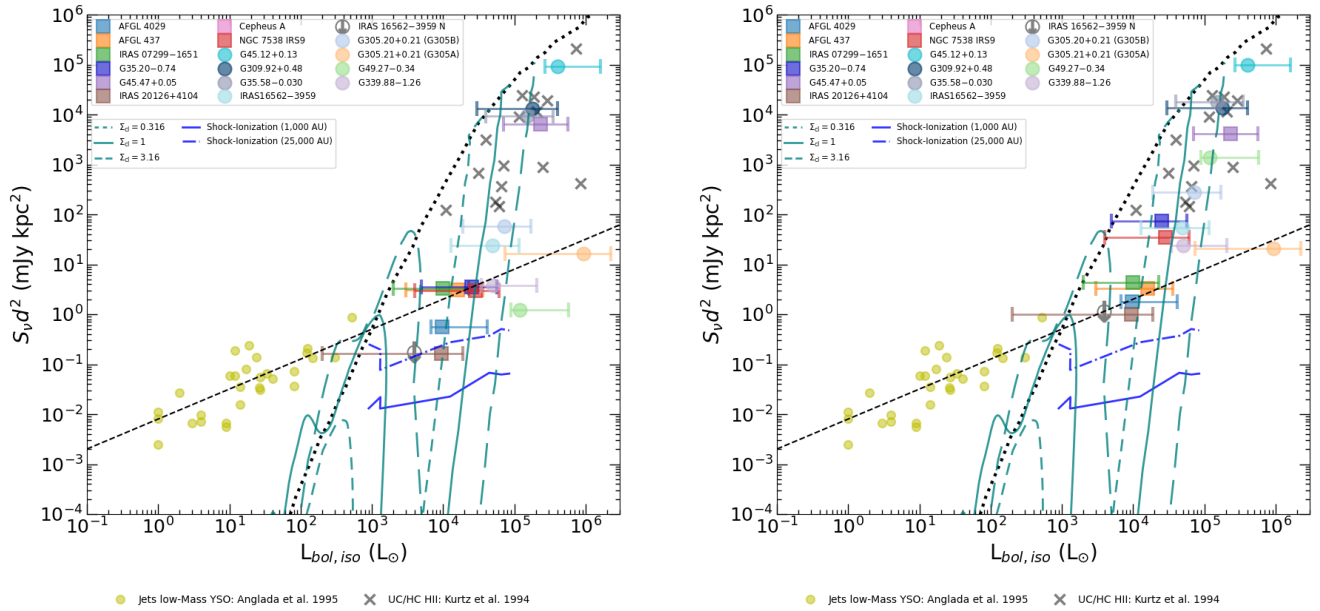


Figure A1. As Fig. 6, but now plotting $L_{\text{bol,iso}}$ for the SOMA sources (left: inner scale, right: SOMA scale).

REFERENCES

- Anglada, G. 1995, in *Revista Mexicana de Astronomia y Astrofisica Conference Series*, Vol. 1, *Revista Mexicana de Astronomia y Astrofisica Conference Series*, ed. S. Lizano & J. M. Torrelles, 67
- Anglada, G., Rodríguez, L. F., & Carrasco-Gonzalez, C. 2015, in *Advancing Astrophysics with the Square Kilometre Array (ASKA14)*, 121, doi: [10.22323/1.215.0121](https://doi.org/10.22323/1.215.0121)
- Anglada, G., Villuendas, E., Estalella, R., et al. 1998, *AJ*, 116, 2953, doi: [10.1086/300637](https://doi.org/10.1086/300637)
- Argon, A. L., Reid, M. J., & Menten, K. M. 2000, *ApJS*, 129, 159, doi: [10.1086/313406](https://doi.org/10.1086/313406)
- Astropy Collaboration, Robitaille, T. P., Tollerud, E. J., et al. 2013, *A&A*, 558, A33, doi: [10.1051/0004-6361/201322068](https://doi.org/10.1051/0004-6361/201322068)
- Astropy Collaboration, Price-Whelan, A. M., Sipőcz, B. M., et al. 2018, *AJ*, 156, 123, doi: [10.3847/1538-3881/aabc4f](https://doi.org/10.3847/1538-3881/aabc4f)
- Azatyanyan, N., Nikoghosyan, E., Harutyunian, H., Baghdasaryan, D., & Andreasyan, D. 2022, *PASA*, 39, e024, doi: [10.1017/pasa.2022.20](https://doi.org/10.1017/pasa.2022.20)
- Bonnell, I. A., Bate, M. R., Clarke, C. J., & Pringle, J. E. 2001, *MNRAS*, 323, 785, doi: [10.1046/j.1365-8711.2001.04270.x](https://doi.org/10.1046/j.1365-8711.2001.04270.x)
- Bonnell, I. A., Bate, M. R., & Zinnecker, H. 1998, *MNRAS*, 298, 93, doi: [10.1046/j.1365-8711.1998.01590.x](https://doi.org/10.1046/j.1365-8711.1998.01590.x)
- Briggs, D. S. 1995, PhD thesis, New Mexico Institute of Mining and Technology
- Brogan, C. L., Hunter, T. R., Cyganowski, C. J., et al. 2016, *ApJ*, 832, 187, doi: [10.3847/0004-637X/832/2/187](https://doi.org/10.3847/0004-637X/832/2/187)
- Carey, S. J., Noriega-Crespo, A., Mizuno, D. R., et al. 2009, *PASP*, 121, 76, doi: [10.1086/596581](https://doi.org/10.1086/596581)
- Caswell, J. L. 1997, *MNRAS*, 289, 203, doi: [10.1093/mnras/289.1.203](https://doi.org/10.1093/mnras/289.1.203)
- Caswell, J. L., Vaile, R. A., Ellingsen, S. P., Whiteoak, J. B., & Norris, R. P. 1995, *MNRAS*, 272, 96, doi: [10.1093/mnras/272.1.96](https://doi.org/10.1093/mnras/272.1.96)
- Cyganowski, C. J., Brogan, C. L., Hunter, T. R., & Churchwell, E. 2009, *ApJ*, 702, 1615, doi: [10.1088/0004-637X/702/2/1615](https://doi.org/10.1088/0004-637X/702/2/1615)
- Cyganowski, C. J., Brogan, C. L., Hunter, T. R., & Churchwell, E. 2011, *ApJ*, 743, 56, doi: [10.1088/0004-637X/743/1/56](https://doi.org/10.1088/0004-637X/743/1/56)
- De Buizer, J. M., Piña, R. K., & Telesco, C. M. 2000, *ApJS*, 130, 437, doi: [10.1086/317351](https://doi.org/10.1086/317351)
- De Buizer, J. M., Walsh, A. J., Piña, R. K., Phillips, C. J., & Telesco, C. M. 2002, *ApJ*, 564, 327, doi: [10.1086/324273](https://doi.org/10.1086/324273)
- De Buizer, J. M., Liu, M., Tan, J. C., et al. 2017, *ApJ*, 843, 33, doi: [10.3847/1538-4357/aa74c8](https://doi.org/10.3847/1538-4357/aa74c8)
- Ellingsen, S. P., Norris, R. P., & McCulloch, P. M. 1996, *MNRAS*, 279, 101, doi: [10.1093/mnras/279.1.101](https://doi.org/10.1093/mnras/279.1.101)

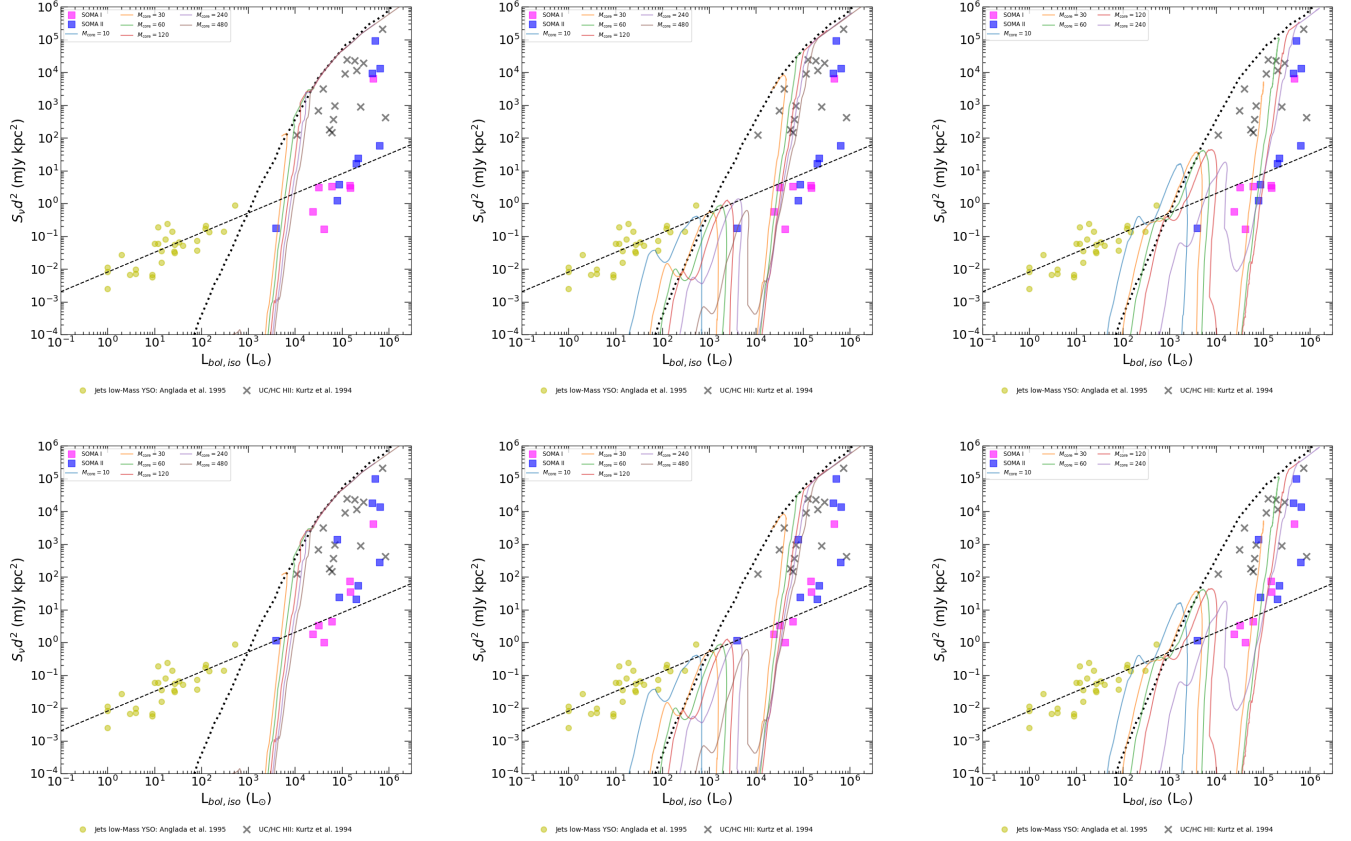


Figure B1. As Fig. 6, but now showing protostellar evolutionary tracks from Zhang & Tan (2018), under the assumption of optically thin radio emission. These models are for $M_c = 10, 30, 60, 120, 240$ and $480 M_\odot$ with $\Sigma_{cl} = 0.316 \text{ g cm}^{-2}$ (left), 1 g cm^{-2} (center) and 3.16 g cm^{-2} (right). Top plots are with the radio luminosity at the inner scale and bottom plots are with the radio luminosity at the SOMA scale.

Fedriani, R., Tan, J. C., Telkamp, Z., et al. 2023, *ApJ*, 942, 7, doi: [10.3847/1538-4357/aca4cf](https://doi.org/10.3847/1538-4357/aca4cf)

Gardiner, E. C., Tan, J. C., Staff, J. E., et al. 2024, *ApJ*, 967, 145, doi: [10.3847/1538-4357/ad39e1](https://doi.org/10.3847/1538-4357/ad39e1)

Ginsburg, A., Darling, J., Battersby, C., Zeiger, B., & Bally, J. 2011, *ApJ*, 736, 149, doi: [10.1088/0004-637X/736/2/149](https://doi.org/10.1088/0004-637X/736/2/149)

Grudić, M. Y., Guszejnov, D., Offner, S. S. R., et al. 2022, *MNRAS*, 512, 216, doi: [10.1093/mnras/stac526](https://doi.org/10.1093/mnras/stac526)

Guzmán, A. E., Garay, G., & Brooks, K. J. 2010, *ApJ*, 725, 734, doi: [10.1088/0004-637X/725/1/734](https://doi.org/10.1088/0004-637X/725/1/734)

Guzmán, A. E., Garay, G., Brooks, K. J., Rathborne, J., & Güsten, R. 2011, *ApJ*, 736, 150, doi: [10.1088/0004-637X/736/2/150](https://doi.org/10.1088/0004-637X/736/2/150)

Guzmán, A. E., Garay, G., Rodríguez, L. F., et al. 2016, *ApJ*, 826, 208, doi: [10.3847/0004-637X/826/2/208](https://doi.org/10.3847/0004-637X/826/2/208)

Guzmán, A. E., Guzmán, V. V., Garay, G., Bronfman, L., & Hechenleitner, F. 2018, *ApJS*, 236, 45, doi: [10.3847/1538-4365/aac01d](https://doi.org/10.3847/1538-4365/aac01d)

Guzmán, A. E., Garay, G., Rodríguez, L. F., et al. 2014, *ApJ*, 796, 117, doi: [10.1088/0004-637X/796/2/117](https://doi.org/10.1088/0004-637X/796/2/117)

Hunter, T. R., Phillips, T. G., & Menten, K. M. 1997, *ApJ*, 478, 283, doi: [10.1086/303775](https://doi.org/10.1086/303775)

Krishnan, V., Ellingsen, S. P., Reid, M. J., et al. 2017, *MNRAS*, 465, 1095, doi: [10.1093/mnras/stw2850](https://doi.org/10.1093/mnras/stw2850)

Krishnan, V., Ellingsen, S. P., Reid, M. J., et al. 2015, *ApJ*, 805, 129, doi: [10.1088/0004-637X/805/2/129](https://doi.org/10.1088/0004-637X/805/2/129)

Kurtz, S., Churchwell, E., & Wood, D. O. S. 1994, *ApJS*, 91, 659, doi: [10.1086/191952](https://doi.org/10.1086/191952)

Liu, M., Tan, J. C., De Buizer, J. M., et al. 2019, *ApJ*, 874, 16, doi: [10.3847/1538-4357/ab07b7](https://doi.org/10.3847/1538-4357/ab07b7)

Liu, M., Tan, J. C., De Buizer, J. M., et al. 2020, *ApJ*, 904, 75, doi: [10.3847/1538-4357/abbebf](https://doi.org/10.3847/1538-4357/abbebf)

McKee, C. F., & Tan, J. C. 2003, *ApJ*, 585, 850, doi: [10.1086/346149](https://doi.org/10.1086/346149)

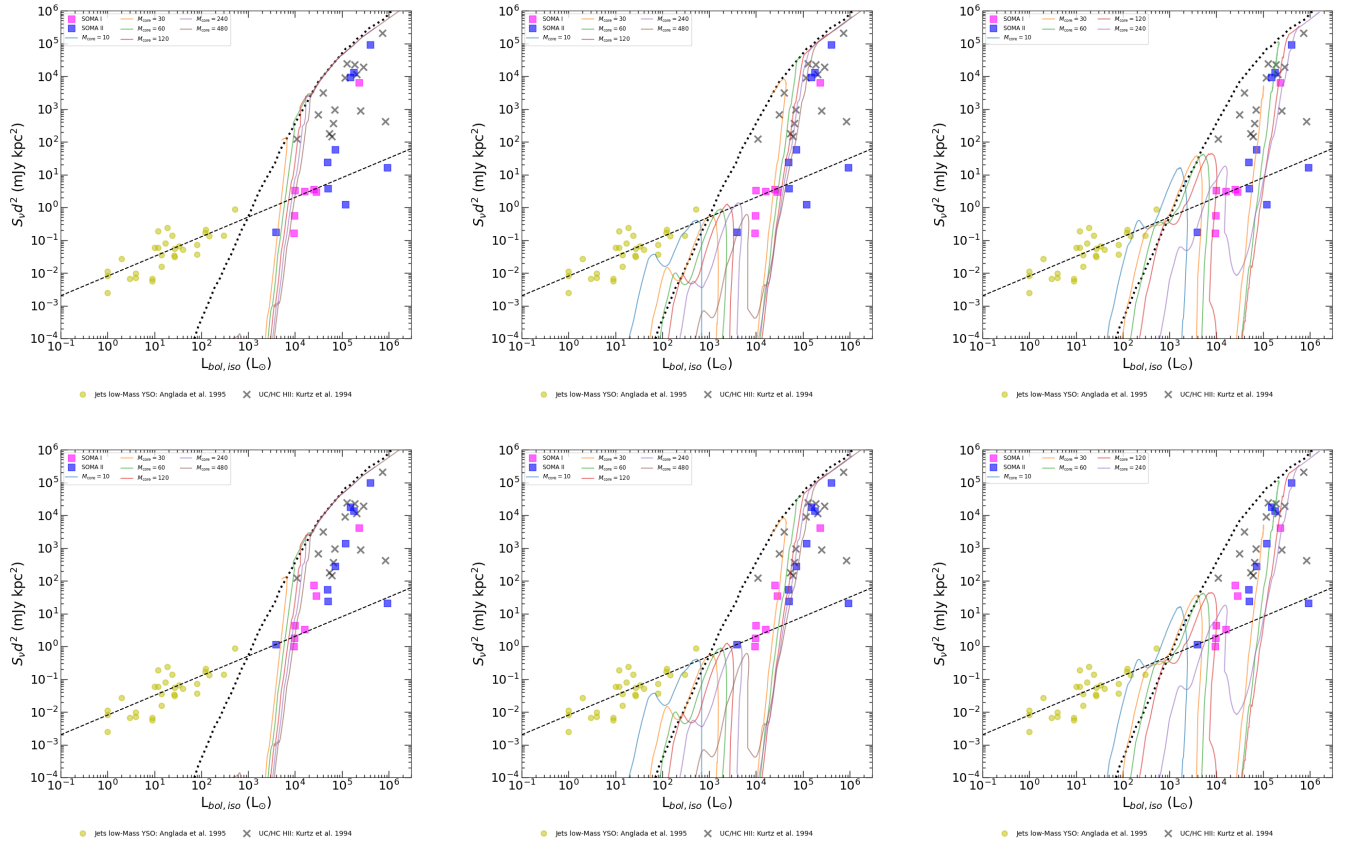


Figure B2. As Fig. B1, but now with the isotropic bolometric luminosity. Top plots are with the radio luminosity at the inner scale and bottom plots are with the radio luminosity at the SOMA scale.

McMullin, J. P., Waters, B., Schiebel, D., Young, W., & Golap, K. 2007, in *Astronomical Society of the Pacific Conference Series*, Vol. 376, *Astronomical Data Analysis Software and Systems XVI*, ed. R. A. Shaw, F. Hill, & D. J. Bell, 127

Mehring, D. M. 1994, *ApJS*, 91, 713, doi: [10.1086/191953](https://doi.org/10.1086/191953)

Montes, V. A., Hofner, P., Oskinova, L. M., & Linz, H. 2020, *ApJ*, 888, 118, doi: [10.3847/1538-4357/ab59cf](https://doi.org/10.3847/1538-4357/ab59cf)

Murphy, T., Cohen, M., Ekers, R. D., et al. 2010, *MNRAS*, 405, 1560, doi: [10.1111/j.1365-2966.2010.16589.x](https://doi.org/10.1111/j.1365-2966.2010.16589.x)

Norris, R. P., Whiteoak, J. B., Caswell, J. L., Wieringa, M. H., & Gough, R. G. 1993, *ApJ*, 412, 222, doi: [10.1086/172914](https://doi.org/10.1086/172914)

Panagia, N. 1973, *AJ*, 78, 929, doi: [10.1086/111498](https://doi.org/10.1086/111498)

Panagia, N., & Walmsley, C. M. 1978, *Astronomy and Astrophysics*, 70, 411

Partridge, B., López-Cañiego, M., Perley, R. A., et al. 2016, *ApJ*, 821, 61, doi: [10.3847/0004-637X/821/1/61](https://doi.org/10.3847/0004-637X/821/1/61)

Pecaut, M. J., & Mamajek, E. E. 2013, *ApJS*, 208, 9, doi: [10.1088/0067-0049/208/1/9](https://doi.org/10.1088/0067-0049/208/1/9)

Phillips, C. J., Norris, R. P., Ellingsen, S. P., & McCulloch, P. M. 1998, *MNRAS*, 300, 1131, doi: [10.1046/j.1365-8711.1998.01979.x](https://doi.org/10.1046/j.1365-8711.1998.01979.x)

Purser, S. J. D., Lumsden, S. L., Hoare, M. G., et al. 2016, *MNRAS*, 460, 1039, doi: [10.1093/mnras/stw1027](https://doi.org/10.1093/mnras/stw1027)

Reynolds, S. P. 1986, *ApJ*, 304, 713, doi: [10.1086/164209](https://doi.org/10.1086/164209)

Robitaille, T. 2019, *APLpy v2.0: The Astronomical Plotting Library in Python*, doi: [10.5281/zenodo.2567476](https://doi.org/10.5281/zenodo.2567476)

Robitaille, T., & Bressert, E. 2012, *APLpy: Astronomical Plotting Library in Python*, *Astrophysics Source Code Library*. <http://ascl.net/1208.017>

Rosero, V., Tanaka, K. E. I., Tan, J. C., et al. 2019a, *ApJ*, 873, 20, doi: [10.3847/1538-4357/ab0209](https://doi.org/10.3847/1538-4357/ab0209)

Rosero, V., Hofner, P., Claussen, M., et al. 2016, *ApJS*, 227, 25, doi: [10.3847/1538-4365/227/2/25](https://doi.org/10.3847/1538-4365/227/2/25)

Rosero, V., Hofner, P., Kurtz, S., et al. 2019b, *ApJ*, 880, 99, doi: [10.3847/1538-4357/ab2595](https://doi.org/10.3847/1538-4357/ab2595)

Simon, R., Jackson, J. M., Clemens, D. P., Bania, T. M., & Heyer, M. H. 2001, *ApJ*, 551, 747, doi: [10.1086/320230](https://doi.org/10.1086/320230)

- Tan, J. C., Beltrán, M. T., Caselli, P., et al. 2014, in *Protostars and Planets VI*, ed. H. Beuther, R. S. Klessen, C. P. Dullemond, & T. Henning, 149–172, doi: [10.2458/azu_uapress.9780816531240-ch007](https://doi.org/10.2458/azu_uapress.9780816531240-ch007)
- Tanaka, K. E. I., Tan, J. C., & Zhang, Y. 2016, *ApJ*, 818, 52, doi: [10.3847/0004-637X/818/1/52](https://doi.org/10.3847/0004-637X/818/1/52)
- Telkamp, Z., Fedriani, R., Tan, J. C., et al. 2025, *The Astrophysical Journal*, 986, 15, doi: [10.3847/1538-4357/adcd79](https://doi.org/10.3847/1538-4357/adcd79)
- Thompson, R. I. 1984, *ApJ*, 283, 165, doi: [10.1086/162287](https://doi.org/10.1086/162287)
- Towner, A. P. M., Brogan, C. L., Hunter, T. R., et al. 2017, *ApJS*, 230, 22, doi: [10.3847/1538-4365/aa73d8](https://doi.org/10.3847/1538-4365/aa73d8)
- Vig, S., Ghosh, S. K., Kulkarni, V. K., Ojha, D. K., & Verma, R. P. 2006, *ApJ*, 637, 400, doi: [10.1086/498389](https://doi.org/10.1086/498389)
- Walsh, A. J., & Burton, M. G. 2006, *MNRAS*, 365, 321, doi: [10.1111/j.1365-2966.2005.09711.x](https://doi.org/10.1111/j.1365-2966.2005.09711.x)
- Walsh, A. J., Burton, M. G., Hyland, A. R., & Robinson, G. 1998, *MNRAS*, 301, 640, doi: [10.1046/j.1365-8711.1998.02014.x](https://doi.org/10.1046/j.1365-8711.1998.02014.x)
- Walsh, A. J., Burton, M. G., Hyland, A. R., & Robinson, G. 1999, *MNRAS*, 309, 905, doi: [10.1046/j.1365-8711.1999.02890.x](https://doi.org/10.1046/j.1365-8711.1999.02890.x)
- Walsh, A. J., Chapman, J. F., Burton, M. G., Wardle, M., & Millar, T. J. 2007, *MNRAS*, 380, 1703, doi: [10.1111/j.1365-2966.2007.12240.x](https://doi.org/10.1111/j.1365-2966.2007.12240.x)
- Wang, P., Li, Z.-Y., Abel, T., & Nakamura, F. 2010, *ApJ*, 709, 27, doi: [10.1088/0004-637X/709/1/27](https://doi.org/10.1088/0004-637X/709/1/27)
- Watson, C., Araya, E., Sewilo, M., et al. 2003, *ApJ*, 587, 714, doi: [10.1086/368286](https://doi.org/10.1086/368286)
- Wood, D. O. S., & Churchwell, E. 1989, *ApJS*, 69, 831, doi: [10.1086/191329](https://doi.org/10.1086/191329)
- Zhang, C.-P., Wang, J.-J., Xu, J.-L., Wyrowski, F., & Menten, K. M. 2014a, *ApJ*, 784, 107, doi: [10.1088/0004-637X/784/2/107](https://doi.org/10.1088/0004-637X/784/2/107)
- Zhang, Y., & Tan, J. C. 2011, *ApJ*, 733, 55, doi: [10.1088/0004-637X/733/1/55](https://doi.org/10.1088/0004-637X/733/1/55)
- Zhang, Y., & Tan, J. C. 2018, *ApJ*, 853, 18, doi: [10.3847/1538-4357/aaa24a](https://doi.org/10.3847/1538-4357/aaa24a)
- Zhang, Y., Tan, J. C., & Hosokawa, T. 2014b, *ApJ*, 788, 166, doi: [10.1088/0004-637X/788/2/166](https://doi.org/10.1088/0004-637X/788/2/166)
- Zhang, Y., Tan, J. C., & McKee, C. F. 2013, *ApJ*, 766, 86, doi: [10.1088/0004-637X/766/2/86](https://doi.org/10.1088/0004-637X/766/2/86)
- Zhang, Y., Tanaka, K. E. I., Rosero, V., et al. 2019a, *ApJL*, 886, L4, doi: [10.3847/2041-8213/ab5309](https://doi.org/10.3847/2041-8213/ab5309)
- Zhang, Y., Tan, J. C., Sakai, N., et al. 2019b, *ApJ*, 873, 73, doi: [10.3847/1538-4357/ab0553](https://doi.org/10.3847/1538-4357/ab0553)